RESOLVED UV AND [CII] STRUCTURES OF LUMINOUS GALAXIES WITHIN THE EPOCH OF REIONISATION

J. Matthee,[1,2,*] D. Sobral,[3] L. A. Boogaard,[2] H. Röttgering,[2] L. Vallini,[2] A. Ferrara,[4,5] A. Paulino-Afonso,[6] F. Boone,[7] D. Schaerer,[8,7] and B. Mobasher[9]

[1] *Department of Physics, ETH Zürich, Wolfgang-Pauli-Strasse 27, 8093 Zürich, Switzerland*

[2] *Leiden Observatory, Leiden University, PO Box 9513, NL-2300 RA, Leiden, The Netherlands*

[3] *Department of Physics, Lancaster University, Lancaster, LA1 4YB, UK*

[4] *Scuola Normale Superiore, Piazza dei Cavalieri 7, I-56126 Pisa, Italy*

[5] *Kavli Institute for the Physics and Mathematics of the Universe (WPI), University of Tokyo, Kashiwa 277-8583, Japan*

[6] *Max-Planck-Institut für Extraterrestrische Physik, Postfach 1312, Giessenbachstr., 85748 Garching, Germany*

[7] *Université de Toulouse; UPS-OMP; IRAP; Toulouse, France*

[8] *Observatoire de Genève, Université Genève, 51 Ch. des Maillettes, 1290 Versoix, Switzerland*

[9] *Department of Physics and Astronomy, University of California, Riverside, CA 92521, USA*

ABSTRACT

We present new deep ALMA and *HST*/WFC3 observations of MASOSA and VR7, two luminous Lyα emitters (LAEs) at $z = 6.5$, for which the UV continuum level differ by a factor four. No IR dust continuum emission is detected in either, indicating little amounts of obscured star formation and/or high dust temperatures. MASOSA, with a UV luminosity $M_{1500} = -20.9$, compact size and very high Lyα EW$_0 \approx 145$ Å, is undetected in [CII] to a limit of $L_{[CII]} < 2.2 \times 10^7$ L$_\odot$ implying a metallicity $Z \lesssim 0.07 Z_\odot$. Intriguingly, our *HST* data indicates a red UV slope $\beta = -1.1 \pm 0.7$, at odds with the low dust content. VR7, which is a bright ($M_{1500} = -22.4$) galaxy with moderate color ($\beta = -1.4 \pm 0.3$) and Lyα EW$_0 = 34$Å, is clearly detected in [CII] emission (S/N=15). VR7's rest-frame UV morphology can be described by two components separated by ≈ 1.5 kpc and is globally more compact than the [CII] emission. The global [CII]-UV ratio indicates $Z \approx 0.2 Z_\odot$, but there are large variations in the UV-[CII] ratio on kpc scales. We also identify diffuse, possibly outflowing, [CII]-emitting gas at ≈ 100 km s^{-1}. VR7 appears assembling its components at a slightly more evolved stage than other luminous LAEs, with outflows already shaping its direct environment at $z \sim 7$. Our results further indicate that the global [CII]-UV relation steepens at SFR < 30 M$_\odot$ yr^{-1}, naturally explaining why the [CII]-UV ratio is anti-correlated with Lyα EW in many, but not all, observed LAEs.

Keywords: galaxies: formation — galaxies: high-redshift — galaxies: ISM — galaxies: kinematics and dynamics —dark ages, reionization, first stars

Corresponding author: J. Matthee
mattheej@phys.ethz.ch

* Zwicky Fellow

1. INTRODUCTION

The advent of the Atacama Large Millimetre Array (ALMA) has enabled the first detailed studies of the interstellar medium (ISM) in various kinds of star-forming galaxies and quasar hosts within the epoch of reionization at $z > 6$ (e.g. Wang et al. 2013; Maiolino et al. 2015; Willott et al. 2015; Inoue et al. 2016; Decarli et al. 2017; D'Odorico et al. 2018). ALMA also opened the opportunity of resolving internal structure at kiloparsec scales (e.g. Jones et al. 2017; Matthee et al. 2017b; Carniani et al. 2018b; Hashimoto et al. 2018a). Currently, ALMA observations of galaxies at $z > 6$ focus on measuring the dust far-infrared (FIR) continuum and FIR fine-structure lines [CII]$_{158\mu m}$ and [OIII]$_{88\mu m}$. The [CII] line partly traces HII regions and neutral gas (i.e. photo-dissociating regions; PDRs; Vallini et al. 2013), while the [OIII] line only traces HII regions. Combined with detailed photoionisation modelling, these lines can be used to constrain gas properties such as the metallicity and ionisation state (e.g. Olsen et al. 2017; Vallini et al. 2017).

While the dust continuum is typically undetected in galaxies selected through their UV or Lyα emission (e.g. Capak et al. 2015; Bouwens et al. 2016b; Pentericci et al. 2016; Matthee et al. 2017b, but see Bowler et al. 2018; Hashimoto et al. 2018a; Tamura et al. 2018 for counter examples), the fine-structure lines are now routinely detected. Due to the low metallicity and higher ionisation state of the ISM in high-redshift galaxies, the [OIII] line may be the strongest far infrared emission line (e.g. Ferkinhoff et al. 2010; Inoue et al. 2016), unlike at low-redshift, where [CII] is typically the strongest (e.g. Stacey et al. 1991; Wolfire et al. 2003; Herrera-Camus et al. 2015). Indeed, recent studies have shown [OIII] to be more luminous than [CII] in objects for which both lines are constrained (Inoue et al. 2016; Carniani et al. 2017; Hashimoto et al. 2018a; Walter et al. 2018).

However, even though being potentially less luminous in high-redshift galaxies, the [CII] line is more easily observed for the vast majority of galaxies currently known at $6 \lesssim z \lesssim 7$. This is because [CII] redshifts into favourable frequencies in ALMA bands 6 and 7 at $z > 5$, while this only happens at $z \gtrsim 8$ for [OIII] (with the exception of a few narrow redshift windows around $z \sim 7$, e.g. Carniani et al. 2017, where the sensitivity to [CII] is still a factor ≈ 2 better). Therefore, practically, observations of the [CII] line are still the least expensive for measuring systemic galaxy redshifts (c.f. Lyα) and studying ISM properties and kinematics.

Some early ALMA observations of galaxies at $z \approx 5-6$ (e.g. Capak et al. 2015) indicated relatively luminous [CII] emission relative to the UV star formation rate (SFR), compared to the observed relation in the local Universe (De Looze et al. 2014). Several other searches at $z \approx 6 - 7$ either found a moderate [CII] deficit (Pentericci et al. 2016; Bradač et al. 2017) or report stringent upper limits on the [CII] luminosity which would place these distant galaxies far below the local relation (e.g. Ouchi et al. 2013; Ota et al. 2014). Such deficit could potentially be due to the prerequisite of a known Lyα redshift, which leads to a bias of observing young, metal-poor systems (e.g. Trainor et al. 2016). New observations of additional galaxies (e.g. Matthee et al. 2017b; Smit et al. 2018; Carniani et al. 2018b; Hashimoto et al. 2018a) and re-analysis of earlier ALMA data (Carniani et al. 2018a) indicate there is more scatter at high-redshift (Carniani et al. 2018b) instead of a strongly preferred low or high [CII]-UV ratio. The [CII]-UV ratio correlates with the relative strength of Lyα emission (Carniani et al. 2018b; Harikane et al. 2018). These measurements are nonetheless complicated by the observation that [CII] is often offset spatially from the UV emission and multiple components of [CII] emission can be associated to UV components (e.g. Matthee et al. 2017b).

In this paper, we present new ALMA and *HST* observations of two very luminous LAEs at $z = 6.5$, named VR7 and MASOSA (Sobral et al. 2015; Matthee et al. 2017a), combined with a multi-wavelength analysis of archival data. While these galaxies have similar Lyα luminosity, the UV continuum is very different, leading to a factor ≈ 5 difference in the equivalent width (EW). What causes these differences in their Lyα EWs? Are the SFRs, dust content and/or ages of the galaxies different? Are there any differences in their metallicities? To answer these questions, we focus on characterising the properties of the ISM (metallicity, kinematics, dust content) and the stellar populations (star formation rate and age), and compare these to other galaxies observed at $z \approx 6 - 7$.

Our targets resemble the Lyα luminosity of the well-known LAEs Himiko and CR7 (Ouchi et al. 2013; Sobral et al. 2015) which are clearly resolved into several components separated by ≈ 4 kpc in both the rest-frame UV and in [CII] emission (e.g. Matthee et al. 2017b; Carniani et al. 2018b; Sobral et al. 2019). Do these luminous LAEs also consist of several components, which could indicate mergers are ubiquitous in the strongest Lyα emitters? We address this with high spatial resolution observations in both rest-frame UV and [CII] emission.

The structure of this paper is as follows. We present the new ALMA and *HST*/WFC3 observations and their data reduction in §2. §3 presents the rest-frame UV and Lyα properties of both galaxies and compares them

to the observed galaxy population at similar lookback time. We then investigate the FIR continuum data from ALMA to constrain the galaxies' dust continuum emission in §4. In §5 we present integrated measurements of the [Cɪɪ] line, while we present the structure in VR7, resolved in both the spatial and spectral dimension in §6. In §7, we discuss the nature of MASOSA and which physical properties determine the [Cɪɪ]/UV ratio in high-redshift galaxies. Finally, we summarise our results in §8. We use a ΛCDM cosmology with $\Omega_\Lambda = 0.70$, $\Omega_M = 0.30$ and $H_0 = 70$ km s^{-1} Mpc^{-1} and a Salpeter (1955) initial mass function. Throughout the paper, UV and IR luminosities are converted to SFR following Kennicutt (1998).

2. OBSERVATIONS & DATA REDUCTION

2.1. *ALMA*

We performed ALMA observations in band 6 of our targets aiming at detecting [Cɪɪ] line emission and FIR dust-continuum emission through ALMA program 2017.1.01451.S in Cycle 5. We observed in four spectral windows: two centred around redshifted [Cɪɪ]$_{158\mu m}$ emission at $z \approx 6.5$ (≈ 252 GHz) and two around 235 GHz, each with a bandwidth of 1875 MHz and 7.8 MHz ($9 - 10$ km s^{-1}) resolution. Both galaxies were observed with 43 antennas in configuration C43-4, allowing baselines from 15 to 783 m, leading to a natural resolution of $\approx 0.4''$. Each galaxy was observed for three executions that consisted of 49 minutes integration time on target, leading to a total on target exposure of 147 minutes.

MASOSA (Matthee et al. 2015; Sobral et al. 2015) was observed during three executions on March 23-24 2018 with precipitable water vapour (PWV) column of 0.9, 1.9 and 2.0mm, respectively. The quasar J1058+0133 was used as atmospheric bandpass and flux calibrator, while quasar J0948+0022 was used as phase calibrator. VR7 (Matthee et al. 2017a) was observed under good conditions (PWV column of 1.0, 1.0 and 0.7 mm, for each execution, respectively) on 6 and 7 September 2018. The quasars J2148+0657 and J2226+0052 were used for atmospheric bandpass and flux calibrator, and phase calibrator, respectively.

The data have been reduced and calibrated using Cᴀsᴀ version 5.1.1-5 following the standard pipeline procedures. The final imaging was performed using the cʟᴇᴀɴ task, with different choices for weighting and tapering depending on the specific scientific question. In general, using natural weighting, we measure a background rms = 6 μJy beam^{-1} in the continuum and a background rms = $1.4 - 1.8$ mJy km s^{-1} beam^{-1} in 18 km s^{-1} channels.

Our analysis and reduction strategy was as follows: we first reduced the data with natural weighting and a UV tapering of 650 kλ (corresponding to an on-sky FWHM of $0.3''$) and by averaging over two velocity channels, leading to a data-cube with a beam FWHM $\approx 0.7 \times 0.7''$ and ≈ 18 km s^{-1} velocity resolution. The tapering was used to optimise detectability of extended emission, while the typical [Cɪɪ] line with FWHM≈ 150 km s^{-1} would still be well resolved. This reduction was used for initial inspection. For detections, we then re-imaged the data with higher spatial resolution (through briggs weighting with robust parameter 0.5 and without tapering) and/or without channel-averaging, with specific parameters chosen optimised for the science question (and motivated in each relevant section independently). For non-detections, we test the robustness of not-detecting the line/continuum by changing the reduction method, and use the tapered reduction motivated by the properties of similar galaxies.

2.2. *HST/WFC3*

We present *HST*/WFC3 observations of MASOSA observed as part of *HST* program 14699 (PI: Sobral) on March 6 2018. Observations were performed for two orbits with the F110W and F160W filters. During each orbit, four exposures of ≈ 650 s were taken following the standard WFC3/IR dither pattern. This results in total exposure times of 5.2ks. We acquire flat-fielded and calibrated ꜰʟᴛ images from the STScɪ server and fix the astrometric solution to the ground-based near-infrared data. Then, after masking bad pixels and cosmic rays, we median combine individual exposures to a final image with $0.064''$ pixel scale with bilinear interpolation using Sᴡᴀʀᴘ (Bertin 2010). We also apply this reduction strategy to the *HST*/WFC3 data on VR7 (originating from the same *HST* program) that was presented earlier in Matthee et al. (2017a). Compared to the previous reduction, the spatial resolution is increased slightly as the image is better sampled. We have verified that the integrated flux and sensitivity are consistent within 5 %.

We use unsaturated, high S/N detections of stars to measure a resolution of FWHM=0.25, $0.28''$ in the F110W and F160W images, respectively. The depth is estimated by measuring the standard deviation of the total counts in 1000 apertures with $0.8''$ diameter placed in empty sky regions. We measure a 3σ limit of F110W= 27.2 and F160W= 26.6 AB magnitude after correcting for aperture losses.

3. THE PROPERTIES OF TARGETED GALAXIES

In this section, we present the general properties of the targeted galaxies based predominantly on Lyα measurements and *HST*/WFC3 data. The measurements are

summarised in Table 1. Our targets have been selected on their high Lyα luminosity ($> 2 \times L^\star$; e.g. Matthee et al. 2015; Konno et al. 2018), a confirmed spectroscopic redshift $z \sim 6.5$ and their observability with ALMA. The Lyα luminosities of our targets are relatively high compared to the majority of earlier ALMA observations, but not extreme (Fig. 1).

MASOSA, at $z = 6.541 \pm 0.001$ (Sobral et al. 2015), is located in the COSMOS field, such that there is *Spitzer*/IRAC data available through the SPLASH program (in particular in the [3.6] and [4.5] bands; Steinhardt et al. 2014). VR7, at $z = 6.534 \pm 0.001$ (Matthee et al. 2017a), is located in the CFHTLS-W4/SA22 field where no deep *Spitzer*/IRAC data is available. Upper limits on rest-frame UV lines besides Lyα based on X-SHOOTER observations (i.e. CIV, HeII, CIII]) are presented for VR7 in Matthee et al. (2017a). The non-detections of high-ionisation lines and the narrow line-widths (< 400 km s^{-1}) indicate that our targets are not powered by a strong active galactic nucleus (AGN; e.g. Sobral et al. 2018.)

3.1. *Lyα luminosity and rest-frame equivalent width*

We measure the Lyα flux using a combination of narrow-band imaging and spectroscopy, which we use to correct for the transmission of the filter at the wavelength Lyα is observed. VR7 and MASOSA have an almost identical integrated Lyα luminosity, while their UV continuum luminosity differs by a factor ≈ 4 (see the next subsection). Measurements of the UV continuum luminosity and the UV slope are used to constrain the continuum around Lyα, and to estimate the EW. The Lyα EW of VR7 is moderate (EW$_0 = 34 \pm 4$ Å), while the EW of MASOSA is extremely high (albeit with large errors; EW$_0 = 145^{+50}_{-43}$ Å). The emission of both Lyα lines consist of a single, clearly asymmetric red peak, with FWHM ranging from 340-390 km s^{-1} Sobral et al. (2015); Matthee et al. (2017a).

3.2. *UV luminosity and colors*

We measure the rest-frame UV luminosity using the *HST*/WFC3 F110W and F160W data. Measurements are performed with 1.2″ diameter apertures to account for the objects sizes and include corrections for missing encapsulated flux based on the WFC3 manual. We correct the F110W photometry for the contribution from Lyα emission based on the measured Lyα luminosity and measure the UV slope β using the F110W-F160W colors following Ono et al. (2010).

For MASOSA, we measure F110W$= 25.74^{+0.13}_{-0.11}$ and F160W$= 25.58^{+0.23}_{-0.20}$. These measurements translate into an absolute UV luminosity M$_{1500} = -20.94^{+0.14}_{-0.13}$ and a
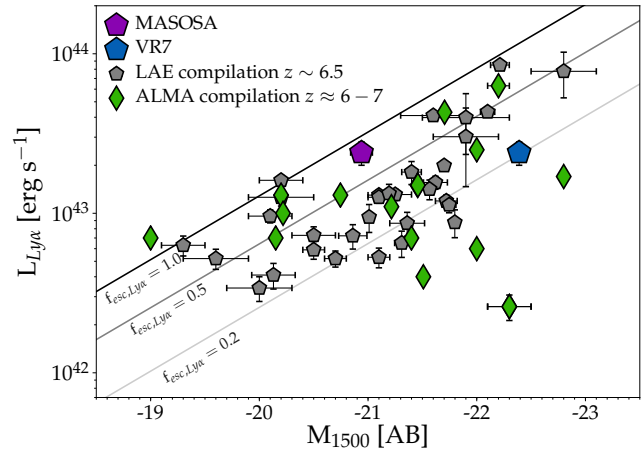

Figure 1. The observed Lyα and UV luminosities of MASOSA and VR7 compared to the galaxy population at $z \approx 6 - 7$. Grey pentagons show a compilation of LAEs from Curtis-Lake et al. (2012); Jiang et al. (2013); Matthee et al. (2017a); Shibuya et al. (2018); Matthee et al. (2018), while green diamonds show galaxies at $z \approx 6 - 7$ targeted by previous ALMA programs as compiled in Appendix C). Solid lines indicate the Lyα escape fraction assuming $\xi_{\rm ion} = 10^{25.4}$ Hz erg^{-1} (e.g. Bouwens et al. 2016a), negligible Lyman-continuum escape fraction and no dust or IGM attenuation. This $\xi_{\rm ion}$ implies an intrinsic Lyα EW=146 Å (Sobral & Matthee 2019). VR7 is among the most UV luminous galaxies targeted by ALMA so far, while MASOSA is among the galaxies with highest Lyα escape fraction.
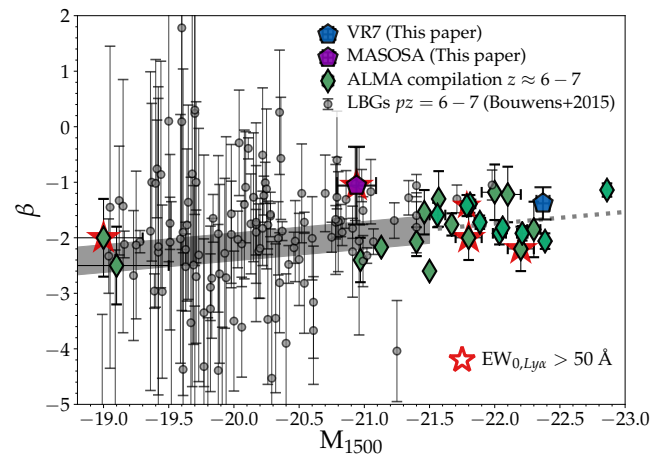
Figure 2. The observed UV slope β and UV luminosities of MASOSA and VR7 compared to our galaxy compilation at $z \approx 6 - 7$ observed with ALMA and to the general Lyman-break population from Bouwens et al. (2015). Red stars highlight sources with the Lyα EW$_0 > 50$ Å. The shaded region shows the fitted relation (Bouwens et al. 2015) and its uncertainty, while we show its extrapolation to higher UV luminosities with a dotted line.
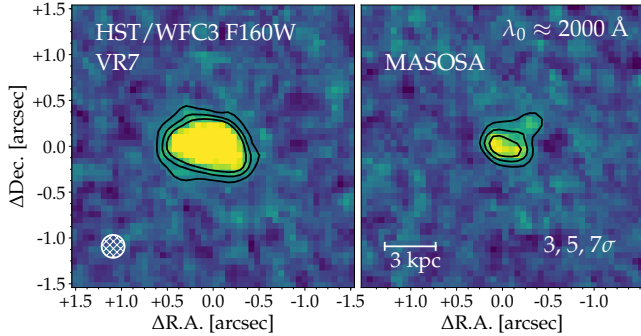
Figure 3. *HST*/WFC3 F160W thumbnail images of VR7 (left) and MASOSA (right) with matched scale and contrast. Contour levels are at 3, 5, 7σ. VR7's UV emission (rest-frame wavelength $\lambda_0 \approx 2000$ Å) is more luminous and more extended than MASOSA. MASOSA is compact, but has an indication of a second component which is only seen in F160W.

red UV slope $\beta = -1.06^{+0.68}_{-0.72}$ (-0.14 magnitude brighter and $\beta_{\rm obs} = -1.49^{+0.56}_{-0.58}$ if we would not correct for the Lyα contribution). The potential red color is intriguing given the high Lyα EW, as the Lyα escape fraction is typically lower for red galaxies (e.g. Matthee et al. 2016). We discuss this in more detail in §7.1.

VR7 is very luminous in the rest-UV, with F110W= $24.35^{+0.05}_{-0.05}$ and F160W= $24.28^{+0.08}_{-0.07}$, which translates in a UV luminosity $M_{1500} = -22.37^{+0.05}_{-0.05}$. VR7 is also relatively red, with $\beta = -1.38^{+0.29}_{-0.27}$, yet in agreement with the observed relation between UV slope and UV magnitude extrapolated to the luminosity of VR7 (Bouwens et al. 2012), see Fig. 2. Due to its lower EW, the correction for the Lyα line has less impact (-0.04 magnitude and $\beta_{\rm obs} = -1.49^{+0.26}_{-0.26}$).

3.3. Rest-frame UV sizes

We measure the de-convolved UV-sizes of MASOSA and VR7 by modelling the light distribution with an exponential profile using the IMFIT software package (Erwin 2015). The PSF image is created by averaging the (normalised) light-profiles of four nearby non-saturated stars and can be modelled accurately with a Moffat profile with FWHM=0.25″. As the morphology in the F110W filter may be affected by Lyα emission, we measure morphology in the F160W filter (see Fig. 3; Appendix B for details on the fitting). For MASOSA, we measure $r_{\rm eff} = 1.12^{+0.44}_{-0.19}$ kpc (corresponding to FWHM=$0.41^{+0.16}_{-0.07}$, arcsec, so marginally resolved in the data) with an ellipticity $0.12^{+0.33}_{-0.12}$ and a position angle $27 \pm 27°$, meaning that the UV-light is almost spherically symmetric. We note that we would measure a slightly smaller size when allowing the Sérsic index to vary ($r_{\rm eff} \approx 0.9$ kpc for $n \approx 0.1$) or when using the

F110W filter ($r_{\rm eff} = 0.87 \pm 0.05$ kpc, indicating relatively compact Lyα emission). While the F160W image hints towards a faint second clump, a two-component exponential does not provide a better fit to the data.

VR7 is well resolved and a single exponential model results in $r_{\rm eff} = 1.56 \pm 0.05$ kpc with PA=80 ± 2 and ellipticity 0.55 ± 0.02. Relaxing the Sérsic index results again in a slightly smaller size ($r_{\rm eff} = 1.52 \pm 0.05$ kpc) with $n = 0.4 \pm 0.08$. In Appendix B we show that the *HST* data from VR7 is better described by two slightly smaller exponential components with a separation of $\approx 0.35″$ (1.9 kpc), but we list the single component fit in Table 1 for consistency with integrated [CII] and UV luminosity measurements.

3.4. How do these galaxies compare to the general galaxy population?

We compare the UV and Lyα luminosities of MASOSA and VR7 to other LAEs identified at $z \sim 6.5$ and to other galaxies at $z \sim 6 - 7$ observed with ALMA (see Appendix C). The latter sample mostly comprises galaxies for which the redshifts have previously been confirmed with (strong) Lyα emission, as ALMA observations require that the redshift is precise to within $\Delta z \approx 0.05$, which is smaller than the typical uncertainty of photometric redshifts. A few notable exceptions include the galaxy B14-65666 at $z = 7.15$ with faint Lyα emission (Hashimoto et al. 2018a) and two Lyman-break galaxies at $z \approx 6.8$ for which the photometric redshift could reliably be estimated (Smit et al. 2018).

As shown in Fig. 1, VR7 is among the most luminous galaxies within the epoch of re-ionisation ever observed with ALMA. MASOSA has a $\lesssim M^\star_{1500}$ luminosity and is among the objects with the highest Lyα EW. We note that the spatial resolution of the ALMA observations presented in this work is a factor ~ 2 higher than most previous observations, allowing more detailed investigation of dynamics and kinematics. The UV sizes of MASOSA and VR7 are comparable to the sizes of other galaxies with similar luminosity (e.g. Shibuya et al. 2015; Bowler et al. 2017).

4. THE FIR CONTINUUM

The ALMA data in the four spectral windows are combined to create 235-250 GHz (1.2 mm) continuum images centred on both objects. These continuum images constrain the FIR continuum luminosity. For VR7, we mask the frequencies where [CII] is detected (see §5), while for MASOSA we use the full frequency range. Several foreground objects are identified in the continuum maps, which can all be associated to objects in either *HST*, *Spitzer* or VLT/MUSE data (Matthee et al. in
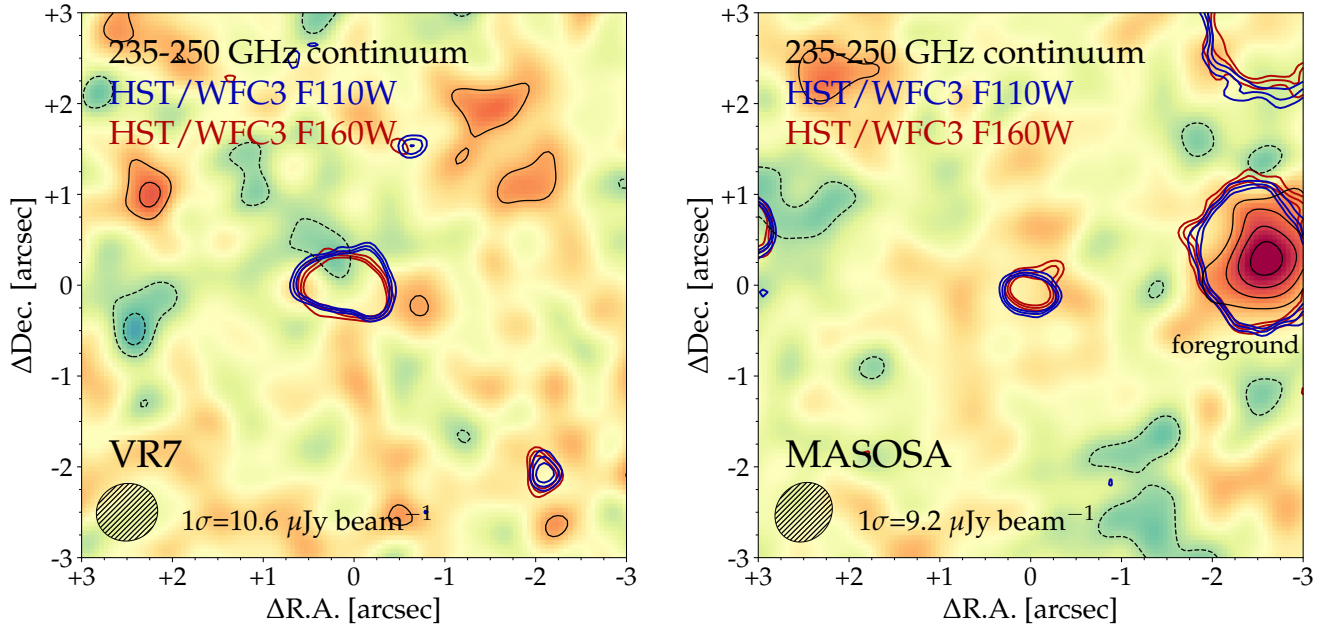
Figure 4. FIR continuum of VR7 (left) and MASOSA (right) in primary beam-corrected data with natural weighting and $0.3''$ taper (beam major-axes of $0.7''$). The black lines show the $\pm 2, 3, 4\sigma$ contours, where the 1σ level ranges from 9.2-10.6μJy beam^{-1}. Dark blue contours illustrate the morphologies in the *HST*/WFC3 F110W band, while dark red shows the F160W band. Both bands trace the rest-frame UV emission. No FIR continuum emission is detected at the locations of VR7 or MASOSA, independent of the data-reduction method.

prep). These objects lie in the foreground of our targets because of detections in images with filters blue-wards of the Lyman-break at $z \approx 6.5$. The foreground objects confirm that the relative astrometry between the ALMA and *HST* data and ground-based imaging is accurate to within $\approx 0.1 - 0.2''$. The general properties of these foreground objects and estimates of their redshifts are summarised in Table A.1.

4.1. *Upper limits at $\lambda_0 \approx 160\mu m$*

No FIR continuum emission is detected at the locations of VR7 or MASOSA (Fig. 4). This result does not depend on the weighting or tapering applied when imaging the visibility data from ALMA, meaning that it is unlikely that flux is resolved out. As source-sizes are $\approx 0.6 - 1.0''$ (major axis) in the rest-frame UV, we use ALMA continuum images constructed with natural weighting and 650 kλ tapering (synthesized beam-FWHM $\approx 0.7''$) to measure physically motivated and conservative upper limits. For VR7, we measure a 1σ limiting $f_{\lambda_0=160\mu m} < 10.6\mu$Jy beam^{-1}, while for MASOSA the 1σ limit is $f_{\lambda_0=160\mu m} < 9.2\mu$Jy beam^{-1}.

We compare our measured upper limits on the continuum flux density around $\lambda_0 = 160\mu m$ with those measured in other galaxies at $z \approx 6 - 7$ in Fig. 5. We show IR flux densities, instead of (temperature dependent) IR luminosities, but note that we corrected

the flux density for CMB heating assuming a dust temperature $T = 45$K, leading to a median correction of ≈ 0.03 dex (da Cunha et al. 2013). We also indicate the expected 1500Å/160μm flux density ratios for local galaxies with extremely low metallicities as inferred from a compilation of galaxies in the local Universe by Maiolino et al. (2015). For comparison, we show the upper limiting flux density ratio for low-metallicity dwarf galaxy I Zw 18, that we determine using measurements from *GALEX*/NUV (Gil de Paz et al. 2007) and *Herschel*/PACS F$_{160}$ (Rémy-Ruyer et al. 2015). This upper limit is comparable to the upper limit for VR7. The IR continuum sensitivity in both MASOSA and VR7 is higher than other galaxies of comparable UV luminosity. VR7 is the most-UV luminous galaxy for which the continuum around $\lambda_0 = 160\mu m$ is currently undetected. This extremely low 160μm/1500Å ratio indicates that VR7 has a lower dust-to-gas ratio and/or higher dust temperature, compared to other luminous galaxies. The only other galaxy with even stronger limits on the 160μm/1500Å flux density ratio is the luminous LAE CR7 (Matthee et al. 2017b).

4.2. *IR luminosity and total SFR*

In order to use these measurements to derive upper limits on the total IR luminosity (L$_{IR}$), one has to make assumptions on the distribution of dust temperatures

that combined result in a modified blackbody spectral energy distribution (SED), as an upper limit at a single frequency can not constrain the shape of this SED. Moreover, at $z \sim 7$ the temperature of the cosmic microwave background is ≈ 20K, which contributes to the heating of dust grains (da Cunha et al. 2013). The choice of (luminosity weighted) dust temperature strongly impacts the integrated IR luminosity. For example, an increase in the dust temperature from 25 to 45 K decreases the limiting L_{IR} by a factor ≈ 4 when the continuum is constrained around $\lambda_0 \approx 160 \mu$m (e.g. Schaerer et al. 2015).

While dust temperatures in typical star-forming galaxies in the $z < 2$ Universe are ≈ 35 K (e.g. Rémy-Ruyer et al. 2013), it is plausible that the dust temperature is higher at higher redshifts, in particular in galaxies with hard ionising sources (i.e. early generations of stars) and a low metallicity (e.g. Cen & Kimm 2014; Maiolino et al. 2015). While direct constraints on the dust temperatures in high-redshift galaxies require large investments of ALMA time (e.g. Bouwens et al. 2016b), Faisst et al. (2017) show that the luminosity-weighted dust temperature in high$-z$ analogues at low-redshift may be as high as 70 K. Behrens et al. (2018) furthermore simulate that intense radiation fields in young galaxies could even result in dust temperatures as high as 90 K.

With these caveats and considerations in mind, we convert our upper limits for VR7 to a limiting $L_{IR,T=45K} < 2.6 \times 10^{10}$ $L_{\odot}$ and $L_{IR,T=45K} < 2.3 \times 10^{10}$ $L_{\odot}(1\sigma)$ for MASOSA integrating a modified black body between 8-1000μm (see Table 1). We assume a dust temperature 45 K and power law exponent $\beta = 1.5$ and correct for the heating from the CMB following Ota et al. (2014), although note these corrections are only a factor ≈ 0.93 and are less important for higher dust temperatures (see Appendix C for more details). The assumed dust temperature is similar to the measured dust temperature in local low-metallicity galaxy I Zw 18 (Rémy-Ruyer et al. 2015). Assuming a dust temperature of 35 K would result in $L_{IR,T=35K} < 1.3 \times 10^{10}$ $L_{\odot}$ and $L_{IR,T=35K} < 1.2 \times 10^{10}$ $L_{\odot}$ for both sources, respectively.

As the observed UV continuum slope correlates with the level of dust attenuation (e.g. Meurer et al. 1999), it is expected that the IR/UV luminosity ratio (the IRX ratio) depends on the UV slope, with the relation being dependent on the shape of the attenuation curve and the dust geometry (e.g. Faisst et al. 2017) and the intrinsic stellar SED (Reddy et al. 2018). We show the locations of VR7 and MASOSA on the IRX-β plane in Fig. 6, together with our compilation of galaxies at $z \approx 6 - 7$,
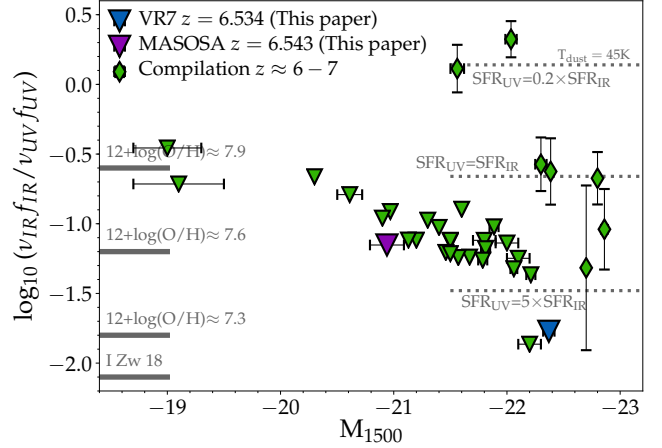
Figure 5. UV continuum luminosity versus the ratio of the UV ($\lambda_0 = 0.15\mu$m) and IR ($\lambda_0 = 160\mu$m) flux densities for the galaxies observed in this paper and a compilation of galaxies observed with ALMA at $z \approx 6-7$. Dotted grey lines indicate the 160μm/1500Å ratiso at which the unobscured SFR are a factor 0.2, 1, 5 times the obscured SFR, assuming a dust temperature of 45 K and Kennicutt (1998) conversions. We indicate the typical gas-phase metallicities measured in galaxies in the local Universe with comparable flux density ratios (based on a compilation by Maiolino et al. 2015) and the upper limit in the extremely low-metallicity galaxy I Zw 18, but stress that the flux ratio is not exclusively metallicity sensitive.
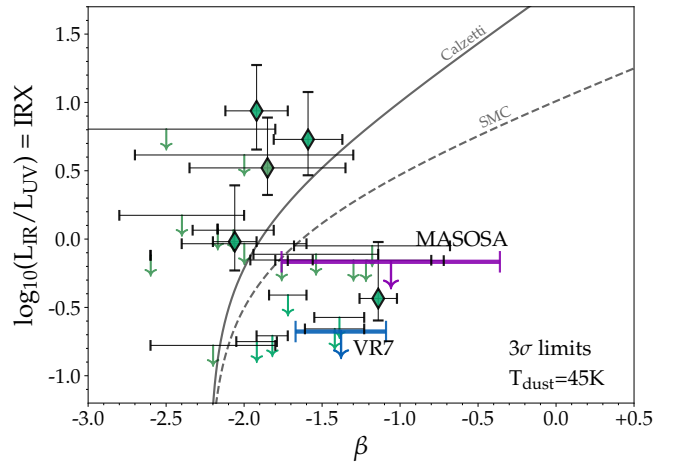
Figure 6. The relation between the IR/UV luminosity ratio (IRX) and the observed UV slope β for our observed galaxies and a compilation of galaxies at $z \approx 6-7$. IR luminosity has been calculated assuming a dust temperature T$=$ 45K, and upper limits are shown at the 3σ level. The solid and dashed line shows the relation for the commonly used Calzetti and SMC extinction curves.
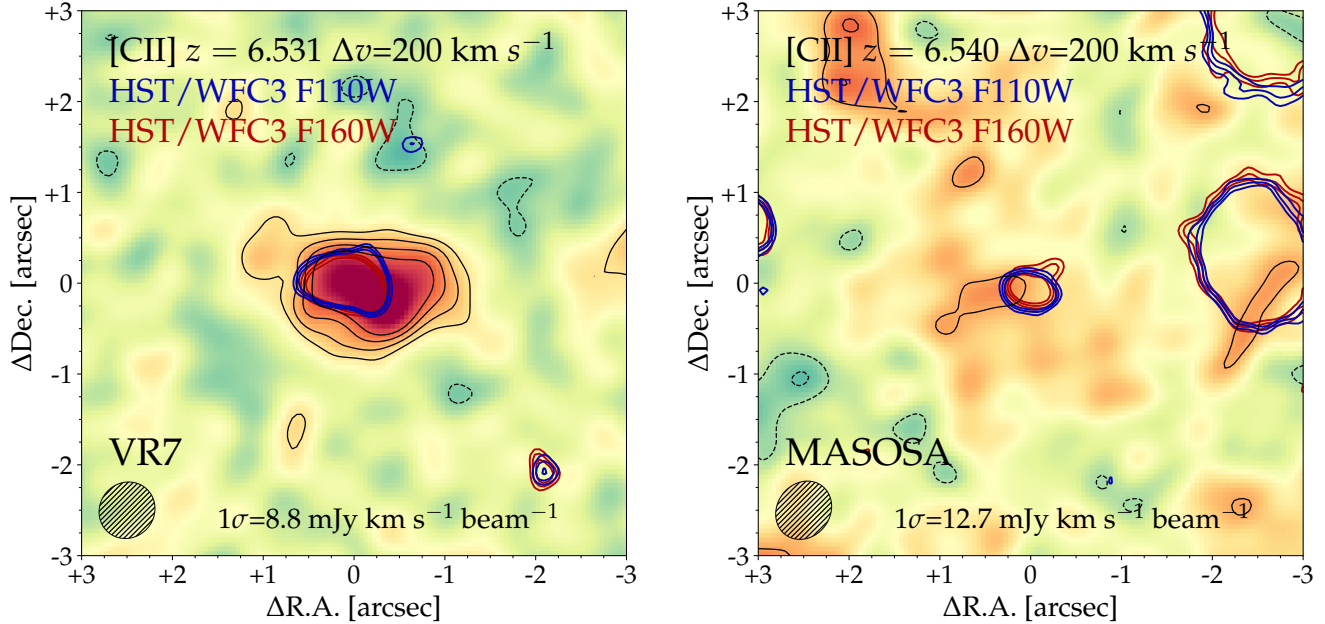
Figure 7. As Fig. 4, but now collapsing frequencies around the [CII] line with VR7 on the left and MASOSA on the right. The beam axes are $0.64'' \times 0.60''$ and $0.67 \times 0.58''$, respectively. Black contours show the $\pm 3, 4, 5\sigma$ level, where $\sigma = 8.8 - 12.7$ mJy km s^{-1} beam^{-1}. Frequencies are collapsed with a width of 200 km s^{-1} around a central frequency that is blue-shifted by 200 km s^{-1} from the Lyα redshift, as motivated in §5. [CII] emission is clearly detected in VR7 (with peak S/N=9.4 and resolved over multiple beams), while we do not detect [CII] emission from MASOSA (see §5.2). Note that the PSF-FWHM of the *HST* imaging is a factor ≈ 2.5 smaller than of this ALMA reduction.

assuming a dust temperature of 45 K. VR7 and MASOSA both lie significantly below the commonly used SMC and/or Calzetti attenuation curves, which could indicate that the dust temperature is higher. Additionally, another explanation could be that dust particles reside relatively closer to the star-forming regions and hence maximise the reddening at fixed IR luminosity (e.g. Ferrara et al. 2017), particularly in compact galaxies.

The constraints on the IR continuum can be converted in an upper limit on the level of obscured star formation. Following Kennicutt (1998), we constrain SFR$_{IR} < 4.6$ M$_\odot$ yr^{-1} and SFR$_{IR} < 4.0$ M$_\odot$ yr^{-1} for VR7 and MASOSA at 1σ respectively for a dust temperature of 45 K. Additionally, we can use the observed UV continuum luminosity as an indicator of the un-obscured SFR. Following again Kennicutt (1998), we measure SFR$_{UV} = 54^{+3}_{-2}$ M$_\odot$ yr^{-1} for VR7 and SFR$_{UV} = 15 \pm 2$ M$_\odot$ yr^{-1} for MASOSA. If we would use the classical method to correct the UV luminosity for dust attenuation based on the observed UV slope (e.g. Meurer et al. 1999), we find SFR$_{dust,Meurer} = 279^{+128}_{-118}$ M$_\odot$ and SFR$_{dust,Meurer} = 208^{+193}_{-171}$ M$_\odot$ yr^{-1} for both galaxies respectively. Such high SFRs are however ruled out by the non-detection of continuum emission in our ALMA observations, which indicate that the fraction of obscured

SFR is $\lesssim 10 - 30$ %.[1] Therefore, combining the limiting obscured SFR as an upper bound to the unobscured SFR, we find SFR$_{UV+IR} = 54^{+5}_{-2}$ M$_\odot$ yr^{-1} for VR7 and SFR$_{UV+IR} = 15^{+4}_{-2}$ M$_\odot$ yr^{-1} for VR7 and MASOSA, respectively.

5. INTEGRATED [CII] EMISSION PROPERTIES

We now focus on the ALMA data around the redshifted [CII]$_{158\mu m}$ frequency. While recent work showed that ALMA resolves [CII] emission in multiple components for a large fraction of high-redshift galaxies (e.g. Matthee et al. 2017b; Carniani et al. 2018b; Hashimoto et al. 2018b), we focus first on the integrated [CII] properties by using a low spatial-resolution reduction of our ALMA data (i.e. synthesized beam FWHM=0.7''), and analyse a higher resolution reduction in §6.

In order to search for [CII] emission, we visually scanned the data-cube in slices of width 18 km s^{-1} from -1000 to +1000 km s^{-1} with respect to the Lyα redshift, and searched for detections within a radius of 3'' (15 pkpc at $z \sim 6.5$). We illustrate the results of this scan

---

[1] We calculate that the obscured SFR would be similar to the unobscured SFR in case the dust temperature is 65 K in MASOSA and 90 K in VR7. Compared to our fiducial calculations assuming T$_{dust} = 45$ K, this would increase the upper limits on the IR luminosity by +0.4 and +1.05 dex, respectively.
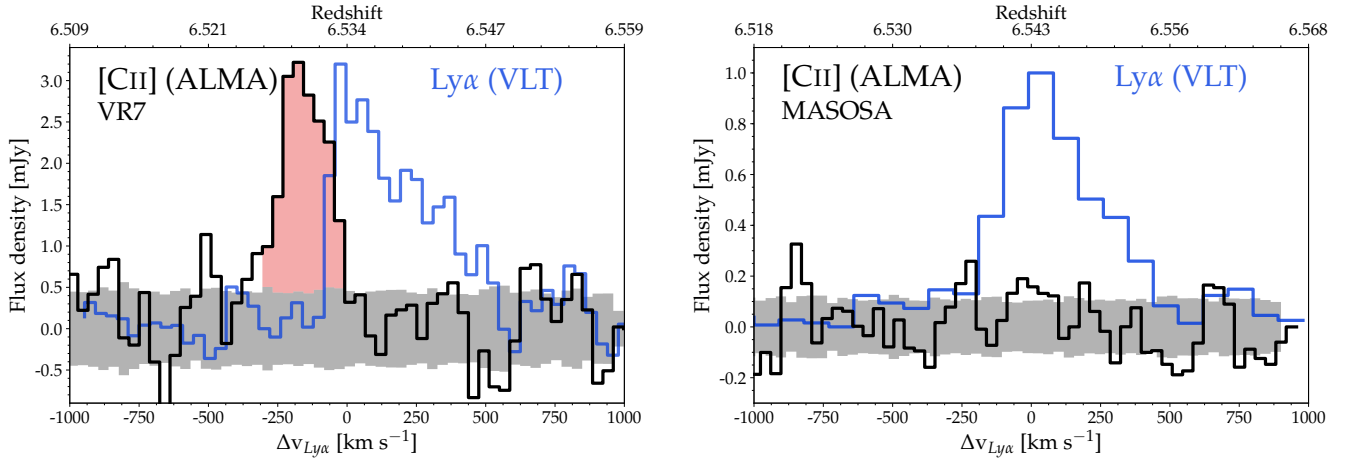
Figure 8. Extracted 1D spectra centered on redshifted [CII] emission with VR7 on the left and MASOSA on the right. The black line shows the ALMA spectrum that is extracted at the rest-frame UV position (see Fig. 7), while the blue line shows the normalised Lyα spectrum. For MASOSA we extract the spectrum within a circular aperture with diameter equal to the beam major axis, while for VR7 we use a aperture that is 1.5 times larger to include extended flux. The noise level of the ALMA data is indicated in grey. Data are binned by a factor two in the frequency direction, resulting in a 38 km s^{-1} velocity resolution. [CII] emission in VR7, detected with integrated S/N≈ 15, is blue shifted with respect to Lyα. The red shaded area highlights the frequency range used to create the integrated [CII] image. We do not detect [CII] emission in MASOSA within 2″ and ±1000 km s^{-1} from Lyα.

in Figs. 7 and 8. Fig. 7 shows collapsed [CII] narrow-band images zoomed at the positions of VR7 and MASOSA, while Fig. 8 shows 1D spectra extracted at the source location. Normalised Lyα spectra are shown on the same barycentric vacuum velocity scale. We clearly detect [CII] emission in VR7, while no [CII] is detected in MASOSA.

5.1. Integrated [CII] properties of VR7

As shown in the left panels in Figs. 7 and 8, the [CII] emission that is detected in VR7 is roughly co-located with the rest-frame UV emission and is slightly blue shifted with respect to Lyα. The peak flux is detected with a S/N=9.4 in the collapsed [CII] image, while the integrated S/N in the 1D extracted spectrum is ≈ 15.

We measure the redshift of peak [CII] emission and the FWHM of the [CII] line as follows. For 1000 iterations, we perturb each data-point in the 1D extraction with its associated uncertainty and measure the frequency where the flux density is highest, and the (linearly interpolated) frequencies where half of the peak flux density is observed. Then, we obtain the median and the 16, 84nd percentiles of those measurements, and find that the peak [CII] flux is observed at $z_{[CII]} = 6.5285^{+0.0007}_{-0.0004}$. This means that the peak of the Lyα emission-line is redshifted with respect to [CII] by $\Delta v_{Ly\alpha} = 217^{+29}_{-19}$ km s^{-1}. The [CII] FWHM is $v_{FWHM,[CII]} = 200^{+48}_{-32}$ km s^{-1}, which is a factor ≈ 1.7 smaller than the Lyα FWHM.

Next, we measure the integrated [CII] luminosity by collapsing the *primary-beam corrected* cube over a wider

range of frequencies (252.285 GHz - 252.519 GHz; corresponding to -20 to -320 km s^{-1} w.r.t. Lyα; illustrated in Fig. 8). We use the IMFIT task in CASA, which fits an elliptical gaussian profile to the data. This results in a total flux of 447 ± 42 mJy km s^{-1} and a de-convolved source size (major/minor axis) $(1.45 \pm 0.14″) \times (0.71 \pm 0.08″)$ with a position angle $96.5 \pm 5.2°$ $((1.58 \pm 0.13″) \times (0.94 \pm 0.06″)$ before deconvolution). Following Carilli & Walter (2013) this flux translates in a [CII] luminosity $4.76 \pm 0.44 \times 10^8$ L$_\odot$, which is emitted over a region of $(7.8 \pm 0.8) \times (3.8 \pm 0.4)$ kpc^2. The integrated [CII] measurements are summarised in Table 1. The [CII] luminosity, line-width and velocity offset to Lyα are similar to other galaxies at $z \approx 6 - 7$ of comparable UV luminosity, and we will discuss this in more detail in §7.3. The major and minor axes of the [CII] emission are larger than the axes of the rest-frame UV emission, which are $(4.6 \pm 0.2) \times (2.1 \pm 0.1)$ kpc^2 when the UV is modeled as a single component. This indicates [CII] is more extended, similar to observations in quasar hosts (Cicone et al. 2015) and a stack of star-forming galaxies (Fujimoto et al. 2019).

The line-width and size can be converted to an estimate of the total dynamical mass following Wang et al. (2013), which results in $M_{dyn}/(\sin i)^2 = 1.4^{+0.4}_{-0.3} - 3.0^{+0.7}_{-0.6} \times 10^{10}$ M$_\odot$ using the semi-minor or semi-major axis, respectively. This mass is a factor $1 - 2$ times the stellar mass estimated in Matthee et al. (2017a).

Table 1. The integrated properties of VR7 and MASOSA as measured from *HST* and ground-based imaging data, optical spectroscopy and ALMA observations. Errors show the 16, 84 percentiles, while upper limits are at the 1σ level. See text in §5.2 that motivates the [CII] luminosity limit for MASOSA.

| Property	VR7	MASOSA
R.A. (J2000)	22:18:56.36	10:01:24.80
Dec.. (J2000)	+00:08:07.32	+02:31:45.34
M_{1500}	$-22.37^{+0.05}_{-0.05}$	$-20.94^{+0.14}_{-0.13}$
β_{obs}	$-1.49^{+0.26}_{-0.26}$	$-1.49^{+0.56}_{-0.58}$
$\beta_{\mathrm{Ly\alpha\ corr.}}$	$-1.38^{+0.29}_{-0.27}$	$-1.06^{+0.68}_{-0.72}$
$r_{\mathrm{eff,UV}}$/kpc	1.56 ± 0.05	$1.12^{+0.44}_{-0.19}$
$L_{\mathrm{Ly\alpha}}$/erg s^{-1}	$2.4^{+0.2}_{-0.2} \times 10^{43}$	$2.4^{+0.4}_{-0.4} \times 10^{43}$
$\mathrm{EW}_{\mathrm{Ly\alpha},0}$/ Å	34^{+4}_{-4}	145^{+50}_{-43}
$z_{\mathrm{Ly\alpha}}$	6.534 ± 0.001	6.543 ± 0.003
$v_{\mathrm{FWHM,Ly\alpha}}$/km s^{-1}	340 ± 14	386 ± 30
[3.6] − [4.5]	-	-0.6 ± 0.2
[CII] and IR properties		
$S_{\nu,\mathrm{fit}}\Delta v$ /mJy km s^{-1}	417.8 ± 80.3	< 12.7
$L_{\mathrm{[CII],CASA}}/10^8$ L$_\odot$	4.76 ± 0.44	< 0.22
$z_{\mathrm{[CII]}}$	$6.5285^{+0.0007}_{-0.0004}$	-
$v_{\mathrm{FWHM,[CII]}}$/km s^{-1}	200^{+48}_{-32}	-
$\Delta v_{\mathrm{Ly\alpha}}$/km s^{-1}	-217^{+29}_{-19}	-
$r_{1/2,major,\mathrm{[CII]}}$/kpc	3.9 ± 0.4	-
$r_{1/2,minor,\mathrm{[CII]}}$/kpc	1.9 ± 0.2	-
$f_{\nu,160\mu m}/\mu$Jy beam^{-1}	< 10.6	< 9.2
Derived properties		
$\mathrm{SFR}_{\mathrm{UV,no\ dust}}$/M$_\odot$ yr^{-1}	54^{+3}_{-2}	15^{+2}_{-2}
$\mathrm{SFR}_{\mathrm{UV,Meurer}}$/M$_\odot$ yr^{-1}	279^{+128}_{-118}	208^{+193}_{-171}
$\mathrm{SFR}_{\mathrm{UV+IR}}$/M$_\odot$ yr^{-1}	54^{+5}_{-2}	15^{+4}_{-2}
EW(Hβ+[OIII])/Å	-	≈ 1500
$Z_{\mathrm{[CII]}}/Z_\odot$	≈ 0.2	$\lesssim 0.07$
$L_{\mathrm{IR,T_d=45K}}/10^{10}L_\odot$	< 2.6	< 2.3
$\mathrm{SFR}_{\mathrm{IR,T_d=45K}}$/M$_\odot$ yr^{-1}	< 4.6	< 4.0
$M_{\mathrm{dyn}}/(\sin i)^2\ 10^{10}$ M$_\odot$	$3.0^{+0.7}_{-0.6}$	-

5.2. *A physically motivated upper limit for the [CII] luminosity in MASOSA*

With the presented observations, no [CII] emission is detected in the LAE MASOSA. Besides the [CII] image collapsed over the frequency range used in Fig. 7, we have also inspected collapsed [CII] images ranging from -1000 to $+1000$ km s^{-1} with respect to the Lyα redshift and with widths ranging from $50 - 500$ km s^{-1}, but none reveal a detection within $2''$ from MASOSA. We have also changed the reduction strategy including no UV tapering to a large UV taper of 200kλ, but none of our attempts resulted in a detection.

We measure the sensitivity of our observations using the r.m.s. value after masking out the position of detected foreground objects. We measure an r.m.s. of 12.7 mJy km s^{-1} beam^{-1} in a collapse of width 200 km s^{-1}, which increases to 20.8 mJy km s^{-1} beam^{-1} collapsing channels over 400 km s^{-1}. The noise increases by a factor ≈ 1.2 when a UV taper of 300kλ is used instead of kλ. As can be seen in Fig. 8, the noise per channel is relatively invariant of frequency, meaning that the sensitivity does not depend on central frequency. These two sensitivities correspond to 1σ limiting [CII] luminosities of $0.14 - 0.22 \times 10^8$ L$_\odot$.

Alternatively, we assess the significance of the non-detection of [CII] in MASOSA by simulating how fake sources with known luminosity, source-size and width would appear in our data. We simulate point-sources with a range of [CII] luminosities and line widths ranging from $100 - 400$ km s^{-1} in reductions with different beam sizes. We place these sources in 500 random positions in our collapsed images and measure the median peak S/N. For an object that is unresolved when imaged with a beam FWHM$> 0.7''$ (corresponding to 3.8 kpc), we measure a S/N of 3 for a luminosity $(0.45, 0.65, 0.90) \times 10^8$ L$_\odot$ for widths $(100, 200, 400)$ km s^{-1}, respectively. If an object is unresolved when imaged with a beam FWHM $> 0.4''$, a S/N of 3 is measured for $(0.38, 0.55, 0.78) \times 10^8$ L$_\odot$ for each respective velocity width. Therefore, variations in the source-size and line width significantly influence the luminosity for which [CII] emission can be detected.

We show in Fig. 9 that the [CII] line FWHM is correlated with the UV luminosity. This correlation resembles the SFR - stellar mass 'main sequence', as the [CII] line-width is expected to be a tracer of gravitational potential and hence mass and the UV luminosity is a proxy for SFR. Increasing scatter in [CII] widths at the brightest UV luminosity could indicate dust attenuation, which could decrease the UV luminosity. MASOSA is among the galaxies with lowest UV luminosity currently targeted by ALMA at $z \approx 6 - 7$ and is thus
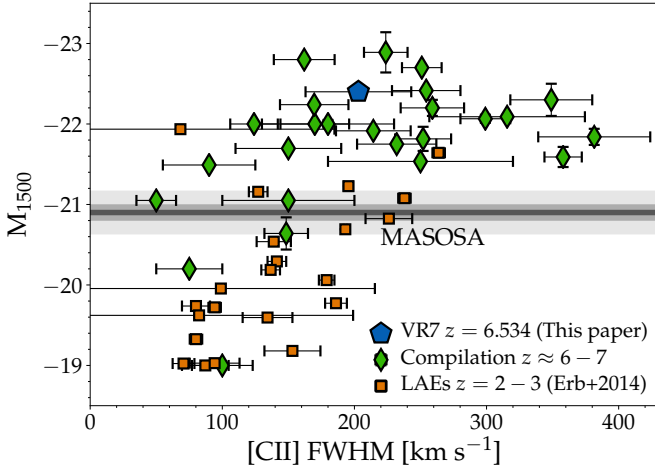
Figure 9. The [Cɪɪ] line FWHM versus UV luminosity for VR7, a compilation of galaxies at $z \approx 6 - 7$ and a sample of LAEs at $z \approx 2-3$ (where we use the line-width of rest-frame optical nebular lines; Erb et al. 2014). UV luminosity, which traces unobscured star formation, is correlated to [Cɪɪ] width, which traces gravitational potential. Therefore, this relation resembles the 'main sequence' between SFR and stellar mass. We highlight the UV luminosity and its uncertainty from MASOSA with a horizontal grey line, indicating that a [Cɪɪ] FWHM of $\approx 120 \pm 80$ km s^{-1} is expected based on the UV luminosity.

expected to have a [Cɪɪ] line width of about $\approx 120 \pm 80$ km s^{-1}. Moreover, in galaxies for which both [Cɪɪ] and Lyα are detected, the [Cɪɪ] width is typically a factor $\approx 0.7 \pm 0.3$ smaller than the Lyα FWHM, likely because the Lyα line width is affected by radiative transfer effects in the ISM and CGM of galaxies. This would point towards a [Cɪɪ] width of ≈ 250 km s^{-1} for MASOSA.

The [Cɪɪ] half-light radius observed in galaxies at $z \approx 6 - 7$ is typically $\approx 2.5 \pm 1$ kpc, a factor ≈ 2 larger than the UV size of these galaxies measured with *HST* (Carniani et al. 2018b). As described above, the UV half-light radius of MASOSA is ≈ 1 kpc. Therefore, a [Cɪɪ] half-light radius of about ≈ 2 kpc is expected for MASOSA, which corresponds to a major axis of $\approx 0.7''$.

Combining the expected [Cɪɪ] extent and line width, the most realistic and conservative estimate of sensitivity of our observations is obtained by assuming a line width of 200 km s^{-1} and using a reduction with beam FWHM $\approx 0.7''$. This implies a 3σ limit for the [Cɪɪ] luminosity from MASOSA of 0.65×10^8 L$_\odot$. We compare this upper limit with expectations from the UV luminosity and its implications in §7.1. For comparison, this value corresponds to $0.3 \times$ L$^\star_{[\mathrm{CII}]}$ in the local Universe (Hemmati et al. 2017).

6. THE RESOLVED STRUCTURE OF VR7
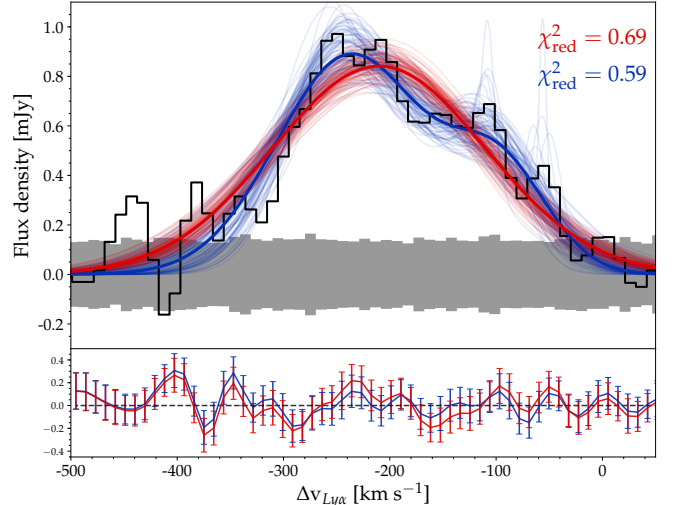


Figure 10. 1D spectrum of the [Cɪɪ] line in VR7, as the left panel of Fig. 8, but without channel averaging, resulting in a ≈ 9 km s^{-1} resolution. The black line shows the measurement, while the grey region illustrates the noise level. We fit the skewed line-profile with a single gaussian component (red) and a combination of two gaussian components (blue). The bottom panel shows the residuals of the best fits. The data marginally prefer a two-component fit, indicating resolved velocity structure.

Table 2. Best-fitted parameters to the two-component gaussian fits of the 1D [Cɪɪ] line profile of VR7 (shown as the solid blue line in Fig. 10).

Property ([Cɪɪ])	Value
Flux$_1$/mJy km s^{-1} beam^{-1}	$139.8^{+29.0}_{-30.3}$
Flux$_2$/mJy km s^{-1} beam^{-1}	$43.1^{+22.9}_{-21.6}$
Flux$_2$/(Flux$_1$+Flux$_2$)	$0.24^{+0.15}_{-0.12}$
$\Delta v_{\mathrm{Ly}\alpha,1}$/km s^{-1}	-211^{+11}_{-9}
$\Delta v_{\mathrm{Ly}\alpha,2}$/km s^{-1}	-87^{+15}_{-15}
FWHM$_1$/km s^{-1}	145^{+41}_{-33}
FWHM$_2$/km s^{-1}	93^{+26}_{-14}

Thanks to the high S/N of the detected [Cɪɪ] line in VR7, we can reduce the ALMA data with a higher spatial resolution and/or relax the velocity-averaging compared to our analysis in §5. In this section, we first investigate the detailed 1D line-profile extracted over the full area over which [Cɪɪ] emission is detected and then focus on resolving structure spatially in both rest-frame UV and [Cɪɪ] emission.

6.1. *1D line modelling*
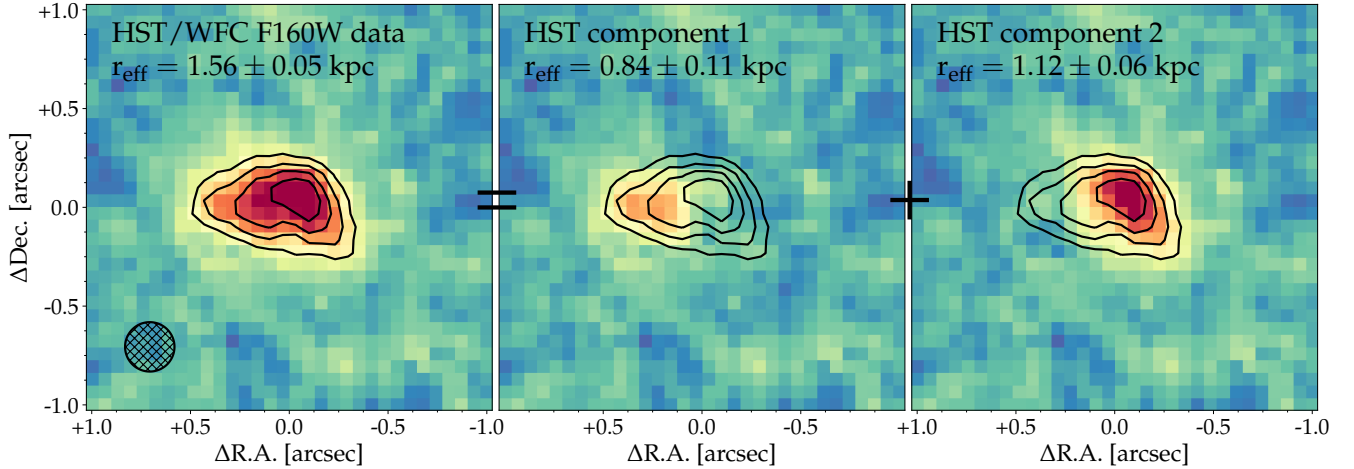
Figure 11. Zoomed-in *HST*/WFC3 image of VR7 in the F160W filter. The left panel shows the data and the size of the PSF-FWHM. The middle and right panels show the individual components of the best-fitted model of two individual exponential components. The contours are drawn in the left panel and shown in the other panels for reference. Each panel lists the effective radius of the respective component, modelled as a single exponential light-profile.

In Fig. 10 we show the 1D line-profile of VR7's [CII] line extracted with the native 9 km s^{-1} resolution and extracted over the full [CII] spatial extent. The line-profile appears asymmetrically skewed towards the red, and is slightly better described by a two-component gaussian than a single gaussian component. The best-fitted values of the two-component gaussian fit are listed in Table 2. The line-profile is characterised by a relatively broad (FWHM=145^{+41}_{-33} km s^{-1}) luminous component and a narrower (FWHM=93^{+26}_{-24} km s^{-1}) component that is a factor ≈ 3 fainter. The narrow component is redshifted by 124^{+19}_{-17} compared to the more luminous component, but still blue-shifted by ≈ 90 km s^{-1} compared to the peak of Lyα emission.

6.2. *Two separate UV components*

VR7's rest-frame UV continuum emission is well resolved in the *HST*/WFC3 image, with a maximum extent of about 1.1″ (≈ 6 kpc) within the 2σ contours. While in general the galaxy is elongated in the east-western direction, it also has a tail extending somewhat to the south-west (see the left panel of Fig. 11). Because of this tail, the rest-frame UV light-profile is better fitted by a two-component exponential model than a single component model (with reduced $\chi^2_r = 1.10$ versus $\chi^2_r = 2.83$, detailed in Appendix B). The best-fitted double exponential model contains two components separated by $0.35 \pm 0.01''$ (1.88 ± 0.07 kpc). We show the individual components in the middle and right panel of Fig. 11. The image for component 1 is created by subtracting the PSF-convolved model of component 2, and vice versa. We list their properties in Table 3. Component 1 lies in the east and is relatively compact, while
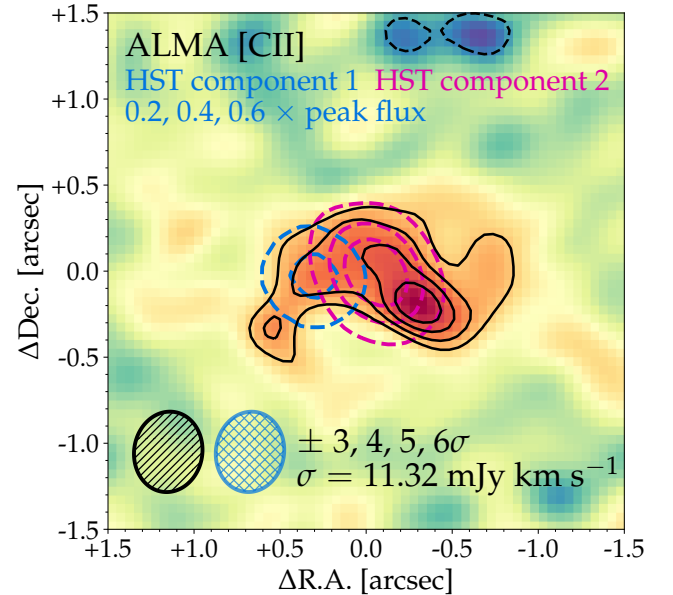
Figure 12. Zoomed-in map of the VR7 galaxy. [CII] image from our high resolution ALMA reduction (beam axes $0.40'' \times 0.47''$), where images are oriented such that east is to the left and north is up. Black lines indicate the $\pm 3, 4, 5, 6\sigma$ contour levels. colored dashed-contours show the individual components in the rest-frame UV identified in *HST*/WFC3 imaging, with a PSF-FWHM matched to the ALMA beam by convolving with a 2D asymmetric gaussian. Like the UV continuum, [CII] extends in the east-west direction following the centers of both components. Higher surface brightness [CII emission is extended to the south-west with a position angle $\approx -45°$, remarkably similar to component 2 in the rest-frame UV. We note that the relative astrometry may have uncertainties on the order $\approx 0.1 - 0.2''$.

Table 3. Best-fitted parameters for the two-component exponential models of the *HST*/WFC3 F160W image of VR7 (shown in Fig. 11). ΔR.A. and ΔDec. are the relative positions with respect to the center listed in Table 1.

| Property	Component 1	Component 2
ΔR.A.	$+0.263''$	$-0.079''$
ΔDec.	$+0.104''$	$+0.126''$
r_{eff}	0.84 ± 0.11 kpc	1.12 ± 0.06 kpc
PA	$76 \pm 9°$	$48 \pm 4°$
Ellipticity	0.52 ± 0.12	0.62 ± 0.08
Fraction of total flux	36 ± 7 %	64 ± 7 %

component 2 coincides with the peak UV emission and is elongated in the south-western direction. Component 2 is slightly larger and a factor $1.8^{+0.7}_{-0.5}$ more luminous, implying that both clumps have very similar SFR surface density. We note that we refrain from over-interpreting the colors of modelled components because of Lyα emission possibly affecting the morphology in the F110W filter, but refer the reader to Appendix B for more details.

6.3. *Spatially resolved [CII] and UV emission*

Now, we focus on spatially resolving the [CII] emission using a high-resolution reduction ($0.40'' \times 0.47''$ beam; 2.2kpc×2.5kpc), see Fig. 12. Extended [CII] emission is observed over an area $\approx 1.3'' \times 0.6''$, with the largest elongation in the east-west direction, similar to what was found above in a lower resolution reduction. Interestingly, higher surface brightness contours are rotated by about 45° clockwise, resembling component 2 in the rest-frame UV. Besides the peak [CII] emission in the west, a hint of a second peak is seen in the east at $\approx -0.5''$ from the image centre. Fig. 12 also compares the [CII] map with the rest-frame UV components identified in the *HST*/WFC3 F160W imaging (Fig. 11). In general, the [CII] morphology is similar to the rest-frame UV, with the major elongation in the east-western direction following the centers of both components. Intriguingly, the peak [CII] emission extends towards the south-west, which is similar to the major direction of elongation of component 2 in the *HST* data.[2]

6.4. *Resolved UV-[CII] ratio*

---

[2] The relative astrometry of the ALMA and *HST* data have been verified with only a single foreground object, meaning uncertainties on the order $\approx 0.1 - 0.2''$ exist. However, the result that the position angles of high surface brightness regions of [CII] and UV emission do not align is robust to these uncertainties.
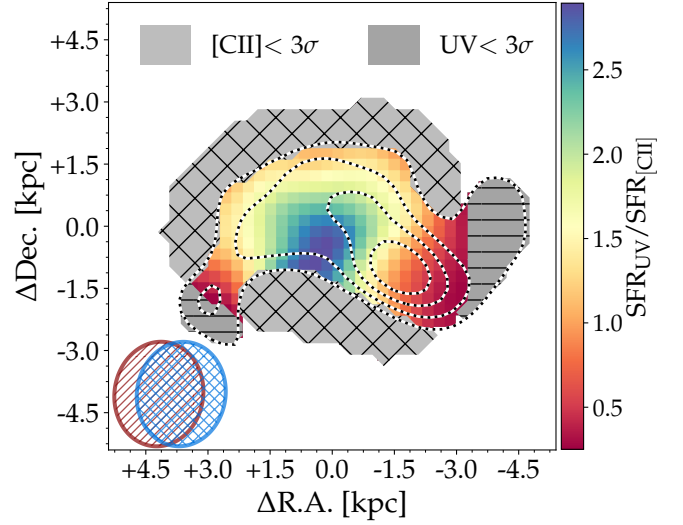
Figure 13. The spatial variation of the $\mathrm{SFR_{UV}}$ to $\mathrm{SFR_{[CII]}}$ ratio, where the first is not dust corrected and the latter estimated from the scaling relation in the local Universe by De Looze et al. (2014). *HST* data have been smoothed to match the ALMA beam. The grey horizontally-hatched region shows where no flux is detected in the rest-UV at $> 3\sigma$, while the cross-hatches highlight where no [CII] flux is detected at $> 3\sigma$. The dotted black-and-white line shows the [CII] level as in Fig. 12.

As a result of the differences in the UV and [CII] morphologies, the UV-[CII] ratio differs within the galaxy. We quantify the variation of the UV-[CII] ratio by converting the luminosities to (unobscured) SFR surface densities following Kennicutt (1998) for the UV and the observed relation between [CII] luminosity and SFR in the local Universe (De Looze et al. 2014) and illustrate the results in Fig. 13.

The average $\mathrm{SFR_{UV}}/\mathrm{SFR_{[CII]}}$ ratio in the region where both UV and [CII] are detected at 3σ is normal, with a mean ratio 1.3 ± 0.1, but the scatter on $\sim$ 2kpc scales is large (0.7). For example, the lowest $\mathrm{SFR_{UV}}/\mathrm{SFR_{[CII]}}$ ratio, observed in the south-western part of the galaxy, is ≈ 0.4, while the highest ratio of about ≈ 2.8 is only 2.8 kpc away. The region with peak [CII] emission has a relatively low UV luminosity, potentially indicating obscured star formation (although no dust is detected in our ALMA observations, see §4) and/or a higher metallicity. We note that the UV colors of component 2 also indicate that it is older and more evolved (see Appendix B), although we stress these colors need to be interpreted cautiously. The central-eastern part of the galaxy has a relatively high UV-[CII] ratio, indicating little obscuration and a low metallicity. No UV emission is detected at the position of the ten-
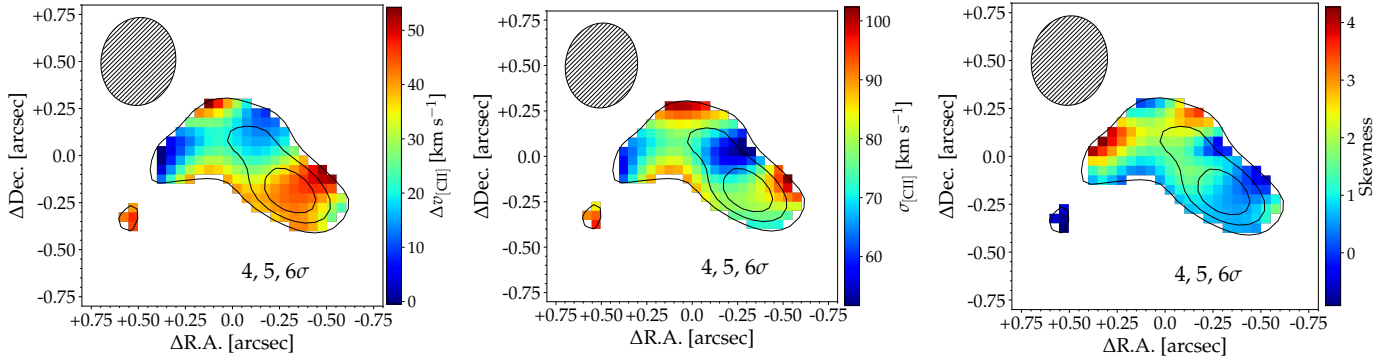
Figure 14. First (left), second (middle) and third (right) moment maps of VR7, based on the highest spatial resolution ALMA reduction and using frequencies within [-320,-20] km s^{-1} with respect to the Lyα redshift. These moments correspond to the velocity map, the dispersion map and the skewness map, respectively. In the left panel, we shift the central velocity to $z = 6.5285$, -217 km s^{-1} compared to Lyα. The moment maps show complex structure and suggest VR7 is dispersion-dominated with a typical $\Delta v/2\sigma \approx 0.3$ in the highest S/N regions.

tative [CII] emitting component in the south-east. The outskirts of the galaxy tend to have a relatively high [CII] luminosity, indicating a strong contribution from PDR emission instead [CII] emission originating from HII regions.

6.5. Velocity structure

6.5.1. Moment maps

Here we explore the velocity structure of VR7 using the first, second and third moment maps of the [CII] emission in the high resolution reduction, which can be interpreted as maps showing the peak velocity, velocity width and line skewness, respectively, see Fig. 14.[3]

The first moment map (left panel in Fig. 14) reveals that the peak velocity varies along the 45° SW axis, the same position angle as component 2. While this pattern somewhat resembles rotation, the maximum velocity difference is only $\Delta v \approx 40$ km s^{-1}, which combined with the velocity dispersion of $\sigma \approx 65$ km s^{-1} results in a kinematic ratio $\Delta v/2\sigma \approx 0.3$. This indicates a dispersion dominated system (e.g. Förster Schreiber et al. 2009), unlike two luminous LBGs observed with ALMA in lower spatial resolution by Smit et al. (2018).

The second moment map (center panel in Fig. 14) shows variations in the velocity dispersion within a factor ≈ 1.5. The region with highest flux density has relatively low dispersion, while the north-east region has

slightly broader line emission. It should be noted that the lowest dispersions in the second moment map are on the order of $\sigma \approx 60$ km s^{-1}, which are similar to the line-width of the dominant (broader) component identified in our fit to the 1D spectrum. This could indicate that the second, narrow and slightly redshifted component identified from the 1D spectrum (Fig. 10) originates mostly from the north-eastern region of the galaxy. This is supported by the line skewness map (right panel of Fig. 14). While the highest skewness values that are found in regions where [CII] is detected at $\approx 4\sigma$ significance should be interpreted with caution, the skewness still increases towards the north-east in the regions with high S/N.

6.5.2. Position-velocity diagrams

We also analyse position-velocity (PV) diagrams in order to study how the [CII] line varies within VR7. We construct PV diagrams by averaging over a slit-width 1.5″ around the center in the NS direction (PA=90°) using the CASA task IMPV. Fig. 15 shows the results for a reduction optimised for high spectral resolution (top row) and high spatial resolution (bottom row), where the first is achieved by reducing the data with normal weighting and UV tapering, while the latter is achieved with briggs weighting, but averaging over two velocity channels.

Fig. 15 confirms the result from the 1D analysis, which is that the [CII] line profile is composed of (at least) two components: a central dominant component that is relatively compact and a redshifted extended component that has a narrower line-width, that we name the *shell* in the rest of the paper. The significance of the shell is $> 4\sigma$ in the reduction with low spatial resolution, but lower in the reduction with higher spatial resolution, which indicates that the [CII] emission is somewhat dif-

---

[3] We note that the simple interpretation of the first and second moments may be somewhat confused by strong line skewness. For example, the first moment of a line-emitting region with fixed central velocity throughout the system, but with a red asymmetry in only part of the system, will show a slight gradient following the skewness gradient, as a red skewed line will result in a higher first moment.
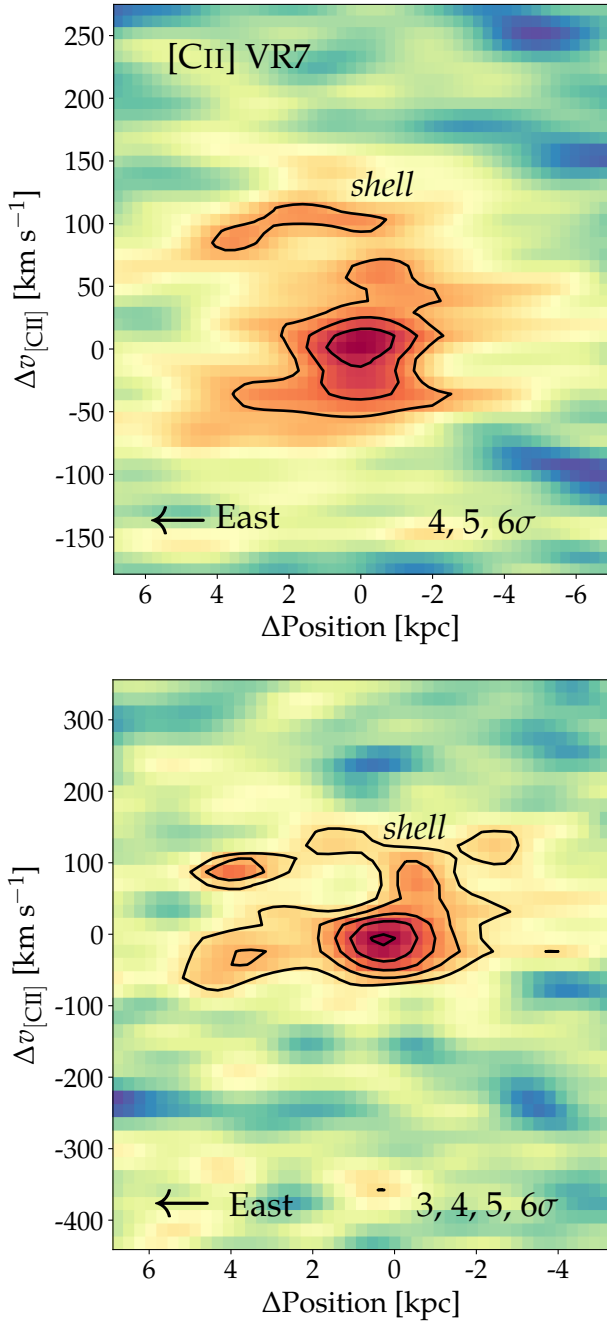
Figure 15. Position velocity diagrams of VR7. The top row uses an ALMA reduction optimised for high spectral resolution but with low spatial resolution (natural weight, UV taper; as Fig. 7). The bottom row uses a high spatial resolution reduction (briggs weight R=0.5; as Fig. 12), but averages over two spectral elements. Flux is averaged over the north-south direction over a 1.5″ width. Note that the y-axis scale differs between top and bottom rows. The top-row shows that the [Cɪɪ] line profile can be resolved in a dominant central component and a faint, diffuse component *shell* at a redshift of ≈ 100 km s^{-1}. This diffuse component is likely resolved out and at lower significance in the high resolution reduction shown in the bottom row.

fuse and resolved out in the latter reduction. The shell is redshifted by ≈ 100 km s^{-1} compared to the central component and is therefore consistent with the narrow gaussian component identified from the integrated 1D spectrum (see Table 2). As the shell is chemically enriched, it is more likely to be outflowing than inflowing. While the flux from the shell extends over roughly the same spatial scales as the central component, the center is shifted slightly towards the north-east, consistent with the skewness map in Fig. 14.

Isolating the dominant component in the bottom panel of Fig. 15, we measure a size FWHM ranging from 0.35-0.50″. As the beam major-axis is 0.46″, this means that the central component is unresolved and has half-light radius $\lesssim$ 1.3 kpc. Combined with the line-width of FWHM=145$^{+41}_{-33}$ km s^{-1}, this results in an estimate of the dynamical mass $M_{\rm dyn}/(\sin i)^2 \lesssim 5.5 \pm 3 \times 10^9$ M$_\odot$ (Wang et al. 2013; Matthee et al. 2017b). Besides the dominant component, the bottom panel of Fig. 15 also hints that there is a second fainter compact [Cɪɪ] emitting component at an offset of about 4 kpc ≈ 0.7″ to the east (see also Fig. 12). The peak flux of this component is a factor two lower than the dominant component and is detected at only ≈ 3 − 4σ significance.

7. DISCUSSION

We now focus on interpreting the ALMA and *HST* observations and place them into the context of other observations. We first address the non-detections of [Cɪɪ] and IR continuum in MASOSA and discuss ways to reconcile this with the potentially red color in the UV (§7.1). Secondly, we discuss the nature of VR7 based on current data in §7.2 and we finally discuss the relation between [Cɪɪ] and UV emission in §7.3.

7.1. *The nature of MASOSA: dusty? Metal poor?*

MASOSA is not detected in [Cɪɪ] or FIR continuum emission. This may be explained by a higher dust temperature combined with a low dust mass and a relatively low metallicity. Such properties are indeed expected given MASOSA's high-redshift and very high Lyα EW (typically found in young, metal poor and dust-free galaxies; e.g. Sobral et al. 2015; Nakajima et al. 2016; Trainor et al. 2016; Sobral et al. 2018).

As illustrated in Fig. 16, the [Cɪɪ] luminosity limits implies that MASOSA is significantly [Cɪɪ]-deficient given its SFR, compared to the typical [Cɪɪ] luminosity found for star-forming galaxies in the local Universe (e.g. De Looze et al. 2014). This can be explained by a lower gas-phase metallicity (e.g. Vallini et al. 2015; Olsen et al. 2017). Following the relations derived by Vallini et al. (2015) based on radiative hydrodynami-

cal simulations, the [CII] upper limit in MASOSA implies a gas-phase metallicity $\lesssim 0.07$ $Z_\odot$ (see Fig. 16) providing further evidence for the very low metallicity of this source as discussed in Sobral et al. (2015). An additional rough metallicity-estimate can be derived based on *Spitzer*/IRAC photometry. For the redshift of MASOSA, the [3.6] band is contaminated by Hβ+[OIII] line-emission, while the [4.5] band includes Hα emission (e.g. Schaerer & de Barros 2009; Raiter et al. 2010a). MASOSA has IRAC magnitudes [3.6] $= 24.0 \pm 0.1$, [4.5] $= 24.6 \pm 0.2$ (Laigle et al. 2016) resulting in the blue color [3.6] $-$ [4.5] $= -0.6 \pm 0.2$. Assuming a flat continuum in the rest-frame optical, this color indicates an EW(Hβ+[OIII])≈ 1500 (e.g. Smit et al. 2014) and hence a gas-phase metallicity $\approx 0.01 - 0.4$ $Z_\odot$ (Castellano et al. 2017). More detailed constraints on the gas-phase metal abundances in the ISM of MASOSA can be obtained from future deep (near-)infrared spectroscopy.

MASOSA's possible red UV slope, $\beta = -1.06^{+0.68}_{-0.72}$, is relatively unexpected given the UV luminosity ($\beta \approx -2.1$; e.g. Bouwens et al. 2012 and Fig. 2), the high Lyα EW (Hashimoto et al. 2017), the blue IRAC colors and the non-detection of dust continuum. Besides dust attenuation that we discussed in §4[4], a red UV slope could be reconciled with a young age in case of a combination of strong nebular continuum emission, strong UV emission lines besides and/or multiple clumps.

For example, Raiter et al. (2010b) show that strong nebular continuum free-free emission can redden the observed UV slope of low metallicity galaxies with hard ionising spectra up to $\beta \approx -1.5$ at $\lambda_0 = 1500$ Å. The most likely emission line boosting the F160W magnitude (and hence the observed β) is CIII]$_{1909}$. CIII]$_{1909}$ is the strongest UV emission line in star-forming galaxies besides Lyα (e.g. Shapley et al. 2003) and can have EW$_0 \approx 10 - 20$ Å (e.g. Rigby et al. 2015; Stark et al. 2015; Maseda et al. 2017), particularly in galaxies with strong Lyα emission (e.g. Le Fèvre et al. 2017). However, we calculate that correcting for a CIII] EW of 25 Å would imply a slope to $\beta = -1.2 \pm 0.7$, meaning that exceptionally strong lines would be required (see also Stroe et al. 2017). Moreover, MASOSA has a slightly different morphology in the reddest *HST* band (e.g. Fig. 3 and Fig. B.2), indicating the presence of a second, relatively faint red clump. Such a clump may be physically disconnected from the youngest stellar population. By fitting the F160W data with a combination of two point

sources[5], we find that the red clump contributes ≈ 20 % of the flux. Reducing the F160W flux by 20 % results in $\beta = -1.5 \pm 0.6$, meaning that the main component of MASOSA can plausibly be 'normally' blue.

Concluding, MASOSA has common properties for galaxies with strong Lyα emission (relatively compact, low metallicity and dust content) and is likely a young star bursting galaxy, with little evidence for being powered by an AGN. While MASOSA's red UV color needs to be verified with deeper observations, a combination of a possible second component, relatively strong rest-frame UV lines such as CIII] and strong nebular continuum emission could reconcile MASOSA's relatively red color with being a young and relatively dust free galaxy.

7.2. *The nature of VR7: hot dust? merger?*

VR7 is a large UV luminous star-forming galaxy with relatively strong Lyα emission, relatively normal [CII] emission. Remarkably, VR7 is the most UV-luminous SFG at $z \approx 6 - 7$ for which no dust emission is detected at 160μm. The limiting 160μm/1500Å flux density ratio is extremely low and in the local Universe only seen for extremely metal poor systems as I Zw 18 (Fig. 5). The Lyα EW implies a Lyα escape fraction of $\approx 15 - 20$ % (Sobral & Matthee 2019), which indicates that a significant fraction of Lyα emission is destroyed by dust. Moreover, the moderate color $\beta \approx -1.4$ also indicates dust attenuation. Therefore, it is likely that dust is present in VR7 at high temperatures (T> 60 K), which would also reconcile the limits on the 160μm continuum flux density with common IRX-β relations (Fig. 6 and e.g. Faisst et al. 2017). The non-detection of IR continuum emission, the narrowness of the [CII] line and the UV morphology all indicate that VR7 is not powered by an AGN (e.g. Ota et al. 2014).

In §6, we showed that the [CII] and rest-frame UV images clearly resolve the light from VR7, with clear indications of multiple components even though they are separated by only $\approx 0.3 - 0.4''$. This separation is a factor 2-3 smaller than the separation of individual components in other luminous Lyα emitter at $z \approx 6.5$ (e.g. Matthee et al. 2017b; Carniani et al. 2018b). Whether the components that are building up the VR7 galaxy are already at a smaller physical separation compared to other luminous LAEs (i.e. VR7 is in a more advanced stage of a merger), or whether this is a viewing angle/inclination effect, can not be addressed with

---

[4] Any significant amount of dust-obscuration in MASOSA would also imply a lower metallicity in order to explain the non-detection of the [CII] line.

[5] The F160W data of MASOSA is described equally well by a single component within the uncertainties, see Appendix B, but we use the results from a two component fit to address the implication of this hypothesis.
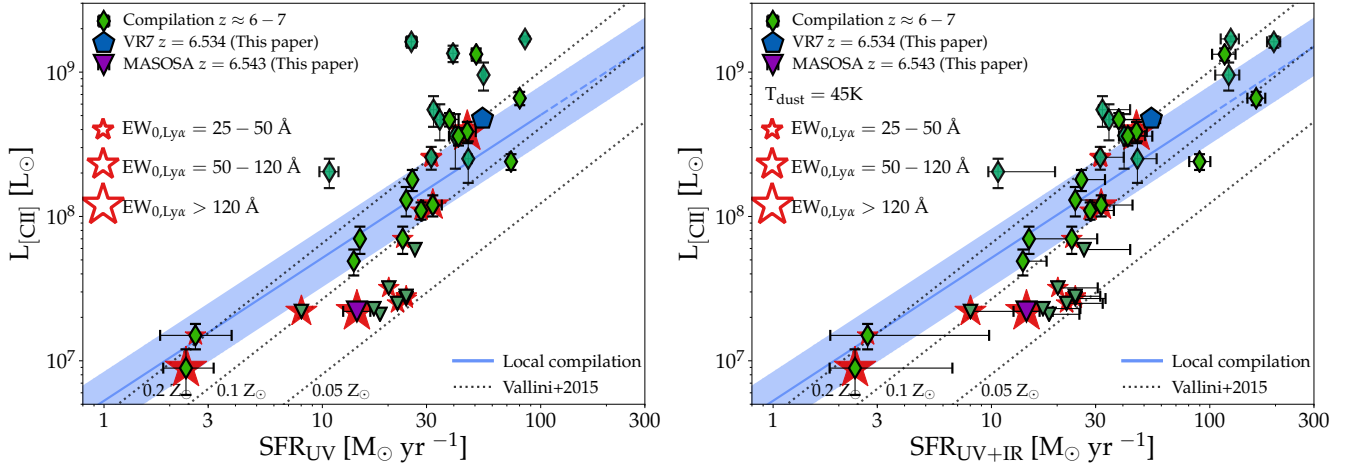
Figure 16. The relation between $\mathrm{SFR_{UV}}$ and [CII] luminosity at $z \approx 6-7$. The *left* panel shows $\mathrm{SFR_{UV}}$ estimated from the rest-frame UV luminosity following Kennicutt (1998). The *right* panel shows $\mathrm{SFR_{UV+IR}}$ where we have converted IR continuum detections to $\mathrm{SFR_{IR}}$ assuming a dust temperature of 45 K and assign the 1σ limiting $\mathrm{SFR_{IR}}$ as an upper error on the SFR as in §4.2. We compare our integrated luminosity measurement for VR7 (blue pentagon) and the upper limit for MASOSA (purple triangle) to other galaxies observed at $z \approx 6-7$ (green diamonds; all computed consistently, see Appendix C) and to the relation observed in the local Universe (De Looze et al. 2014; blue band; where the shaded region shows the dispersion, the line-style changes to dashed at the luminosities were relations are extrapolated and the relation is shifted to the same IMF as used here). Upper limits are at the 1σ level. We indicate galaxies with strong Lyα lines with red stars. Dotted lines show the relation between [CII] luminosity and SFR at different gas-phase metallicities inferred from hydrodynamical simulations by Vallini et al. (2015), which used the same IMF as our analysis.

the current data. Interestingly, among the luminous LAEs targeted with ALMA so far, VR7 has the lowest Lyα EW, which could indicate it is in a slightly more evolved stage than LAEs with higher Lyα EW. A slightly more evolved stage is also in line with its moderate UV slope, particularly since the other luminous LAEs have $\beta \approx -2$.

7.3. *What determines the [CII]/UV ratio*

Here, we address the relative [CII] and UV luminosities of galaxies at $z \approx 6-7$, compared to galaxies in the local Universe. Earlier work either found relatively high (Capak et al. 2015), moderately low (Pentericci et al. 2016) or extremely low [CII] luminosities at fixed $\mathrm{SFR_{UV}}$ (e.g. Ota et al. 2014). As detailed in Appendix C, we homogenise the measurements by converting all UV luminosities to $\mathrm{SFR_{UV}}$ consistently and we revise upper limits following the method applied to MASOSA. Our results are compared to relations between [CII] luminosity and SFR based on observations of galaxies in the local Universe (De Looze et al. 2014). Like our observations, we rescale the relation to the common SFR calibration of Kennicutt (1998). The results are shown in Fig. 16, where the left panel uses SFR estimated from only the UV, while the right panel uses the information on the dust continuum provided by ALMA to correct for obscured SFR.

While VR7 has an integrated [CII]-$\mathrm{SFR_{UV}}$ ratio that is very similar of other galaxies with similar SFR[6], MASOSA is [CII] deficient, similar to several other galaxies with $\mathrm{SFR_{UV}} \approx 10-20 \ \mathrm{M_\odot \ yr^{-1}}$. There is significant dispersion in [CII] luminosities at fixed $\mathrm{SFR_{UV}}$, particularly in the range $\mathrm{SFR} \approx 30-60 \ \mathrm{M_\odot \ yr^{-1}}$ that includes most of the objects currently observed. A part of this dispersion is related to variation in relative strengths of Lyα emission, since the SFR-[CII] ratio is anti-correlated with the observed Lyα EW (e.g. Carniani et al. 2018b; Harikane et al. 2018). Indeed, a large fraction of objects with [CII] deficits are strong Lyα emitters (Fig. 16). Furthermore, among the sample of luminous LAEs known at $z \approx 6-7$, MASOSA is at the higher end of the Lyα EW distribution (e.g. Fig. 1), in agreement with this picture. On the other hand, Fig. 16 shows that several other strong Lyα emitters, such as CR7 (Matthee et al. 2017b), have rather typical [CII] luminosities given the SFR.

In the range $\mathrm{SFR_{UV+IR}} \approx 30-200 \ \mathrm{M_\odot \ yr^{-1}}$, the detected galaxies at $z \approx 6-7$ are roughly co-located with galaxies in the local Universe and follow a similar slope $\log_{10}(\mathrm{L_{[CII]}}) \propto \log_{10}(\mathrm{SFR})$ once obscured SFR is

---

[6] We note that the global $\mathrm{SFR_{UV}}$ and [CII] surface densities of VR7 also agree with galaxies in the local Universe observed by De Looze et al. (2014).

accounted for. At SFRs below 30 M$_\odot$ yr^{-1} the results are less clear, as the [CII] line is undetected in a large fraction of galaxies, with a 1σ limiting luminosity well below the local relation.

If relatively faint [CII] lines are confirmed in these systems, it would imply that the relation between [CII] luminosity and SFR steepens at low SFRs and that a larger fraction of the ISM is ionised. This potentially indicates a stronger correlation between gas-phase metallicity and SFR in lower mass galaxies. Alternatively, it could also indicate more bursty star formation in fainter galaxies (leading to a higher ionisation parameter) or other differences in ISM properties. Such a steepening is observed in the local Universe using a sample of low-metallicity dwarf galaxies (De Looze et al. 2014). Furthermore, such steepening would also explain why relatively low [CII] luminosities are found among most strong Lyα emitters, as the fraction of galaxies with strong Lyα emission is higher at low SFRs in the observed sample (Fig. 16). This picture simultaneously allows higher [CII] luminosities in the most luminous Lyα emitters found in the large wide-field surveys (e.g. Matthee et al. 2017b; Carniani et al. 2018b).

8. CONCLUSIONS

In this paper, we have presented new deep follow-up observations of two luminous Lyα emitters at $z \approx 6.5$ with *HST*/WFC3 and ALMA with a resolution of 1.5-2 kpc. The *HST* data are used to characterise the strength and morphology of rest-frame UV emission, constraining the un-obscured SFR. ALMA data are used to constrain FIR dust continuum emission and measure the strength and dynamics of the atomic [CII]$_{158\mu m}$ fine-structure line. The targeted galaxies, VR7 and MASOSA (Sobral et al. 2015; Matthee et al. 2017a), have a high $\approx 2 \times L^\star$ Lyα luminosity, while their UV luminosity differs by a factor four. Table 1 summarises our measurements. Our main results are the following:

1. VR7 is among the most luminous and largest star-forming galaxies known at $z \approx 6 - 7$ with an unobscured SFR=54^{+3}_{-2} M$_\odot$ yr^{-1} and an extent of ≈ 6 kpc at the 2σ level. VR7 has a typical moderate color given its high UV luminosity, $\beta = -1.38^{+0.29}_{-0.27}$, and moderate Ly$\alpha$ EW$_0 = 34$ Å. The *HST*/WFC3 rest-frame UV data of VR7 strongly prefers a two-component exponential model over a single component model. The individual components are separated by 1.88 ± 0.07 kpc and have sizes r$_{\rm eff} = 0.84 \pm 0.11$ kpc and r$_{\rm eff} = 1.12 \pm 0.06$ kpc. The larger component is a factor $1.8^{+0.7}_{-0.5}$ more luminous and is elongated in the south-western direction.

2. MASOSA, which has a slightly sub-L* UV luminosity (unobscured SFR=15^{+2}_{-2} M$_\odot$ yr^{-1}) and a normal size (r$_{\rm eff} = 1.12^{+0.44}_{-0.19}$ kpc), is among the galaxies with highest Lyα EW known at $z \approx 6 - 7$ (EW= 145^{+50}_{-43} Å). Surprisingly, MASOSA seems to have a relatively red UV continuum color $\beta = -1.06^{+0.68}_{-0.72}$, which could indicate strong CIII] line-emission, nebular continuum emission and/or a multiple component nature.

3. No dust continuum emission is detected in either VR7 or MASOSA (§4.2). Unless the dust temperature is very high (T$_{\rm dust} \gtrsim 60$K), this indicates little amounts of dust present in both systems. VR7 has an extremely low L$_{\rm IR}$/L$_{\rm UV}$ ratio, similar to the ratio of the extremely metal poor dwarf galaxy I Zw 18 and the luminous LAE CR7 (Matthee et al. 2017b). Assuming T$_{\rm dust} = 45$K, we find that the obscured SFR in both galaxies is a small fraction of the unobscured SFR ($\lesssim 10$ % and $\lesssim 30$ %, respectively).

4. Our ALMA data reveals a strong [CII] emission detection in VR7 (S/N=15), but none in MASOSA (§5). VR7 has a typical integrated [CII] luminosity relative to its SFR, indicating a metallicity ≈ 0.2 Z$_\odot$. For MASOSA, we derive a physically motivated [CII] upper limit that results in a [CII] deficit given the SFR$_{\rm UV}$ and that implies a very low metallicity < 0.07 Z$_\odot$. Combining our measurements with a large compilation, we find indications that the relation between [CII] luminosity and SFR steepens at SFRs $\lesssim 30$ M$_\odot$ yr^{-1}, which could be explained due to a tighter correlation between SFR and metallicity in these galaxies compared to more luminous systems. Such a correlation naturally explains why most galaxies with high Lyα EW have relatively low [CII] luminosity.

5. [CII] emission in VR7 is extended (major/minor axes $(7.8 \pm 0.8) \times (3.8 \pm 0.4)$ kpc^2), a factor ≈ 1.8 larger than the UV emission. The faint and low surface brightness [CII] emission extends mostly in the east-west direction. The high surface brightness [CII] emission also extends 45° towards to south-west (§6). We find that the UV-[CII] ratio varies significantly within the galaxy (up to factors of ≈ 7 on ≈ 3 kpc scales). The dominant [CII] emitting component is compact, with an estimated half-light radius $\lesssim 1.3$ kpc and being slightly offset from the peak UV emission. We find that some faint, diffuse [CII] emission is red-shifted by $+100$ km s^{-1} with respect to the central

component, possibly indicating an outflow and explaining the skewness and asymmetry seen in the 1D spectrum. Finally, we find indications for a second compact component at a 4 kpc separation.

Our observations show that there is little dust present in luminous Lyα emitters at $z \approx 6 - 7$, unless the dust has very high temperatures ($\gtrsim 60$ K). Future ALMA surveys should therefore aim at observationally constraining these temperatures by performing deep observations at higher frequencies. There are large variations in the [CII] luminosities of galaxies at $z \approx 6 - 7$ which are strongly related to the SFR$_{UV}$, albeit with significant scatter. Deep ALMA observations of galaxies with SFR$_{UV} < 10$ M$_\odot$ yr^{-1} (M$_{1500} \gtrsim -20$) should test whether the relation between [CII] luminosity and SFR$_{UV}$ indeed steepens at low SFRs. ALMA and *HST* are capable of resolving the most luminous systems at $z \approx 6 - 7$ and reveal that they are actively assembling from multiple components with strong variations in the SFR$_{UV}$-[CII] ratio, while their environment is already being influenced by galactic outflows. In the future, resolved rest-frame optical spectroscopy using integral field unit spectroscopy on *JWST* will provide crucial complementary measurements of the ISM metallicity, the contribution from non-thermal emission and the masses, ages and metallicities of stellar populations.

Table A.1. Global properties of foreground objects. Continuum flux is measured using the primary beam corrected map, while the S/N is measured before the primary beam correction.

R.A.	Dec.	$f_{\nu,250\mathrm{GHz}}$	S/N	Comment
(J2000)	(J2000)	(μJy beam^{-1})		
10:01:24.705	+2:31:32.73	1212	56.0	Dusty, highly obscured star forming galaxy with unknown photo$-z$. Detected in the *Spitzer*/IRAC [3.6] and [4.5] bands, but not detected in optical bands or our *HST*/WFC3 imaging data.
10:01:25.427	+2:31:45.23	138	8.2	In the centre of a relatively nearby face-on spiral galaxy at $z = 0.131$ with identifier SDSS J100125.41+023145.2.
10:01:24.629	+2:31:45.62	64	5.0	Galaxy with photo$-z = 1.46 \pm 0.05$ and $\mathrm{M_{star}} = 10^{10.37 \pm 0.08}$ M$_\odot$, ID 810182 in Laigle et al. (2016) $\approx 2''$ away from MASOSA.
22:18:57.117	+0:08:03.79	55	4.2	Detected in *HST*/WFC3 with F110W=24.4. Marginally detected in a combined *griz* image. No emission-line detected in MUSE (Matthee et al. in prep). Likely photo-$z \approx 1.5 - 2.8$.
22:18:57.143	+0:08:18.29	79	3.5	Associated(?) with a LAE identified in MUSE $z_{Ly\alpha} = 3.062$, offset $0.25''$ to the north-west

Facilities: ALMA, *HST* (WFC3), VLT (FORS2, MUSE, X-SHOOTER).

Software: astropy, (Astropy Collaboration et al. 2013), imfit (Erwin 2015), matplotlib (Hunter 2007),
Topcat (Taylor 2013), Scipy (Jones et al. 2001–), Swarp (Bertin 2010)

APPENDIX

A. CONTINUUM DETECTIONS IN THE ALMA DATA

Besides our targets, our continuum maps reveal a number of detections, see Fig. A.1. Three objects are detected in the MASOSA pointing with S/N ranging from 5-56, while two objects with S/N 3.5-4.2 are (tentatively) detected in the VR7 pointing, see Table A.1 for details. In the MASOSA field, the highest S/N detection is likely a dusty and highly obscured star-forming galaxy, as it is not detected in optical imaging (limiting AB magnitudes ~ 28) nor in the *HST*/WFC3 data presented here. The object is detected in the MIR *Spitzer*/IRAC [3.6] and [4.5] bands, showing it is very red. No [CII] or any other emission line is detected in the ALMA data, indicating it is not at similar redshift as MASOSA. The second most luminous continuum detection coincides with the centre of a face-on spiral galaxy with an SDSS-redshift of $z = 0.131$. The third continuum detection (with a S/N=5.0) is relatively near MASOSA (at $\approx 2.5''$, see also the right panel in Fig. 4), but coincides with a galaxy with photometric-redshift $z = 1.46 \pm 0.05$ in the Laigle et al. (2016) catalogue. The continuum detections in the VR7 field are of lower significance. The detection with S/N=4.2 is shown in the left panel of Fig. A.1 and is co-located with a faint galaxy in the *HST* data. No emission-line is detected in our MUSE data (Matthee et al. in prep), suggesting that the galaxy is below $z < 3$ (otherwise Lyα could have been detected) and above $z > 1.5$ (otherwise [OII] could have been detected). The other continuum detection may be associated to a LAE at $z = 3.062$, although it is offset by $0.25''$ to the north-west.

B. FITTING REST-FRAME UV SIZES

Here we provide more details on the fitting of the *HST*/WFC3 data, in particular on fitting VR7 as a single component or a two component model and the fitting results for MASOSA.

B.1. *Single component versus two component in VR7's HST data*

As described in the main text (§3.3), we find that the light profile of VR7 in the *HST*/WFC3 F160W data is better described by a combination of two exponential profiles than by a single exponential (or Sérsic) profile. The result of the fitting using IMFIT (Erwin 2015) is shown in Fig. B.1. The residual map of the single-component fit shows clear structure at the $\approx 3\sigma$ level, while residuals of such strength are not seen in the more flexible two-component fit.
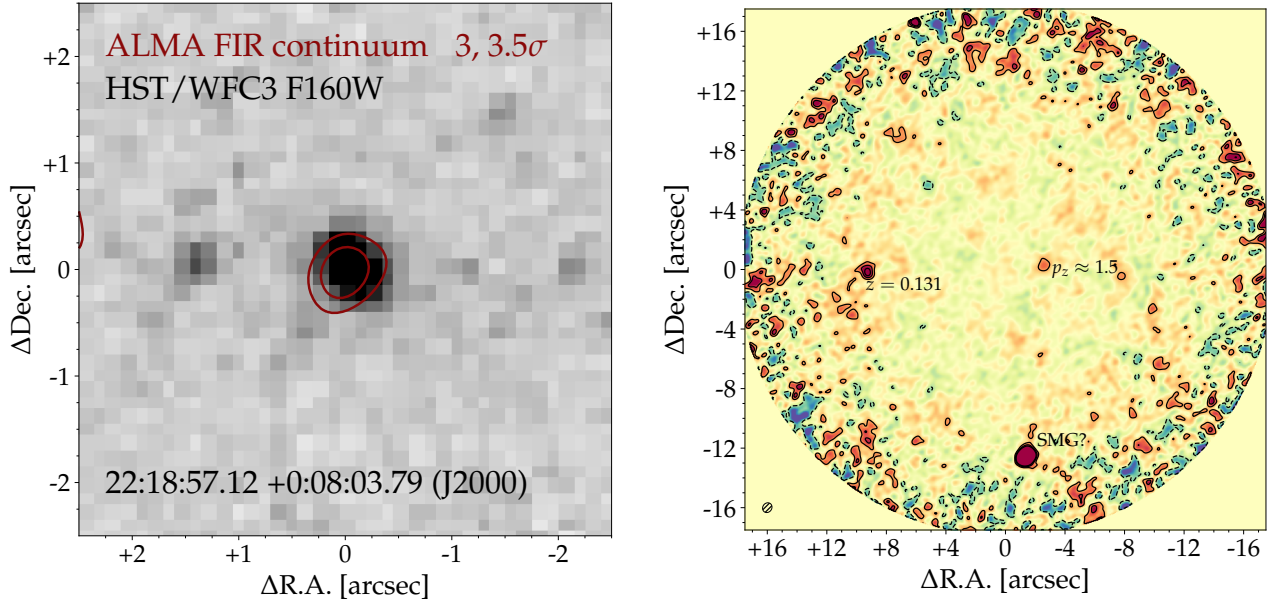
Figure A.1. Continuum maps of foreground sources in the field of VR7 (left) and MASOSA (right). For VR7 we zoom in on the foreground source detected with S/N=4.2 and show that the IR continuum contours coincide well with the *HST*/WFC3 position. For MASOSA we show our full primary-beam corrected image and highlight the positions of the three foreground sources, where contour levels are at the 4, 8, 12σ level.

We note that the F110W data (which morphology is possibly affected by Lyα emission) is also better described by a two-component fit, although the relative flux and sizes of the two component reverse (i.e. a larger and more luminous component in the east and a smaller fainter component south-west). While this implies a color gradient, we note that these (and particularly their uncertainties) are challenging to quantify without strong priors such as assuming that the relative sizes, position angles and ellipticities are the same and assuming a homogeneously distributed Lyα surface brightness. If we use the morphology of the individual components in the F160W data as a prior and assume Lyα emission is homogeneously distributed, we measure that the flux fraction in component 1 (Fig. 11) is 42 ± 6 % and 36 ± 7 % in the F110W and F160W data, respectively. This implies component 1 has a UV luminosity and color $M_{1500} = -21.41 \pm 0.17$ and $\beta = -2.04^{+0.89}_{-0.95}$, while component 2 has $M_{1500} = -21.77 \pm 0.12$ and $\beta = -1.14 \pm 0.62$. Without subtracting Lyα emission from the F110W flux density the UV slopes would be bluer, with $\Delta\beta \approx -0.3$.
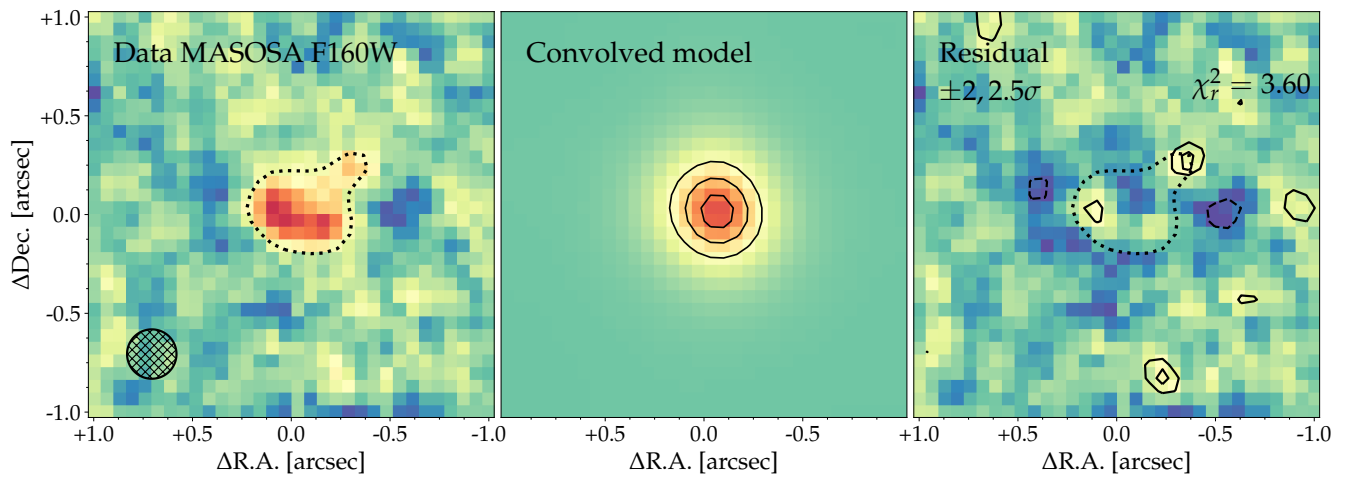
B.2. *Single component in MASOSA*

We show our best fit single exponential model to the F160W from MASOSA in Fig. *B.2*. Due to the limited S/N of the galaxy the data can not reliably distinguish between a single component or a combination of two components, although visually a hint of a second component can be seen in the north-west of the galaxy. Deeper *HST* data is required to confirm this component.

C. COMPILATION AND HOMOGENISATION OF MEASUREMENTS FROM GALAXIES AT $Z \approx 6 - 7$

In order to compare our measurements to earlier observations of galaxies at $z \approx 6 - 7$, we compile a sample of spectroscopically confirmed galaxies at $z \approx 6 - 7$ for which the [CII] line and adjacent continuum has been observed with ALMA. This compilation includes LAEs (Ota et al. 2014; Inoue et al. 2016; Matthee et al. 2017b; Carniani et al. 2018a), UV-selected galaxies confirmed through Lyα emission (Maiolino et al. 2015; Willott et al. 2015; Pentericci et al. 2016; Carniani et al. 2018b; Hashimoto et al. 2018a), lensed UV-selected galaxies (Knudsen et al. 2016; Bradač et al. 2017) and UV-selected galaxies confirmed through [CII] emission (Smit et al. 2018). We also include the sample of LBGs, LAEs and galaxies selected through their photometric redshift at $z \approx 5.7$ from Capak et al. (2015) with updated measurements from Barisic et al. (2017). For a proper comparison, we collect observed properties (i.e. UV, [CII] and Lyα luminosity, line-widths and IR flux densities) and self-consistently convert these to derived properties (i.e. star formation rates and IR luminosities). Table *C.1* shows the observed properties of the galaxies at $z \approx 6 - 7$, while Table *C.2* lists derived properties. The Lyα properties are listed in Table *C.3*.
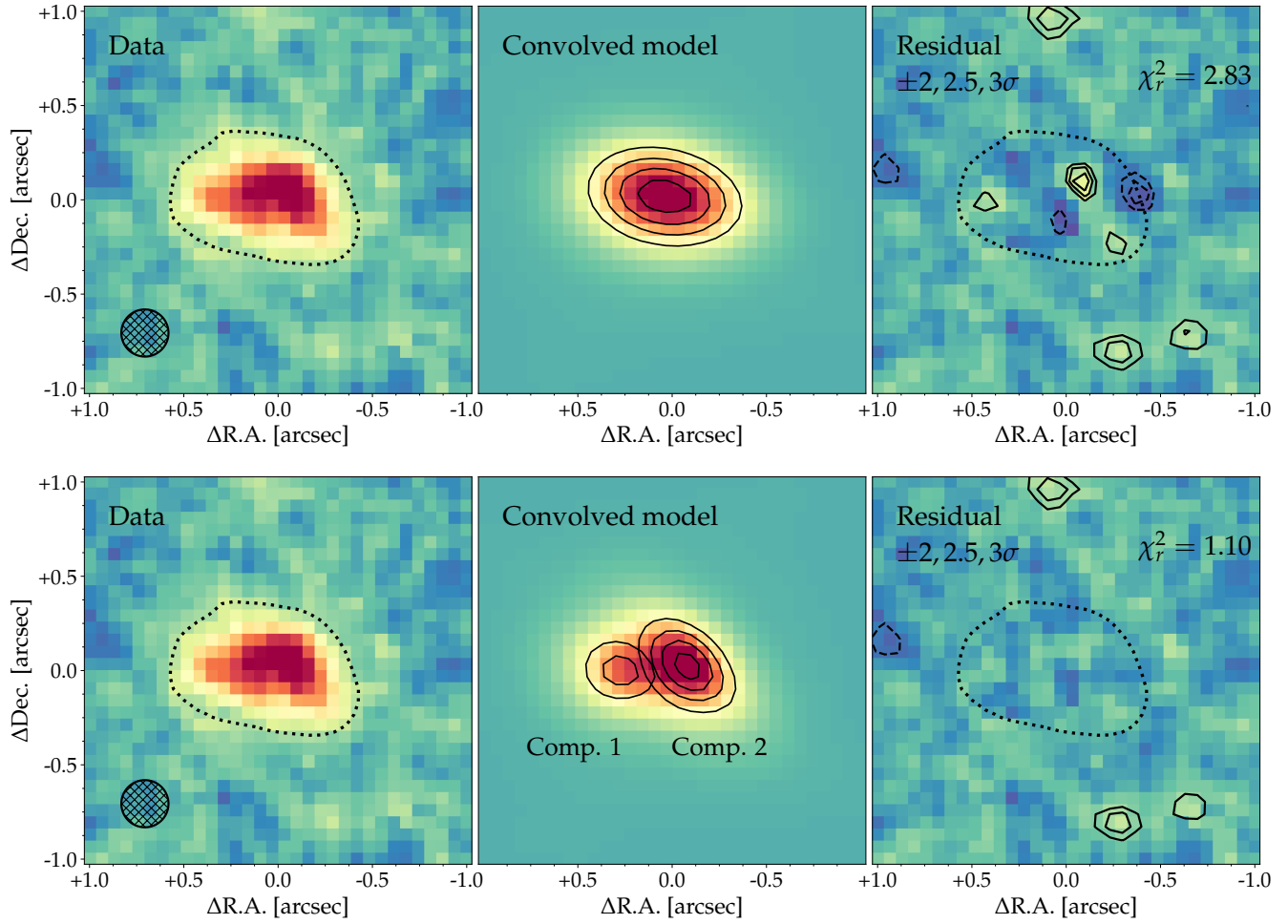
Figure B.1. Zoomed-in *HST*/WFC3 image of VR7 in the F160W filter. The left panel shows the data and the size of the PSF-FWHM. The middle panels show the models and the right panels show the residuals. The top row shows a single exponential light-profile, while the bottom row shows a combination of two exponential light-profiles. For reference, the dotted contour illustrate the outline of the galaxy. Reduced χ^2 values are computed within the dotted contour-level. The rest-frame UV light-profile of VR7 is better described by two individual components.

Figure B.2. As Fig. *B*.1, but showing the single component exponential fit to MASOSA.

We use published values of M_{1500} and β wherever possible, but for several objects we calculated M_{1500} based on published photometry. When available, Lyα luminosities have been computed using published line-flux measurements. For galaxies in which no [CII] is detected, we measure the physically motivated upper limit similar to the procedure in §5.2. This means that we estimate the expected line-width based on the UV luminosity (typically 150-200 km s^{-1}) and convert published noise values to this width assuming rms$_{[CII]} \propto \sqrt{\Delta v_{\text{channel}}}$, where $\Delta v_{\text{channel}}$ is the channel width over which the noise is measured. Measurements of/upper limits on the continuum flux at $\lambda_0 = 160\mu m$ (typically $\lambda_{obs} = 1.2$mm) have been converted to an FIR ($\lambda = 42.5 - 122.5\mu m$) and IR ($\lambda = 8 - 1000\mu m$) luminosity following Ota et al. (2014), after correcting the contribution from CMB heating following da Cunha et al. (2013). We assume a modified blackbody of the form: $B_\nu = \frac{M_{\text{dust}}\kappa}{D_L^2} \frac{2h\nu^3}{c^2 e^{\frac{h\nu}{k_B T_d}} - 1}$, where D_L is the luminosity distance, k_B the Boltzmann constant, T_d the dust temperature, M_{dust} the dust mass, $\kappa = \kappa_{850}(\frac{\nu}{\nu_{850}})^\beta$, where κ_{850} is the dust opacity at 850 μm, which we assume is 0.077 m^2 kg^{-1} similar to Ota et al. (2014) and β is the grey-body power-law exponent, which we assume to be $\beta = 1.5$ following Ota et al. (2014). Then, the obscured SFR is calculated following Kennicutt (1998): $\log_{10}(\text{SFR}_{\text{IR}}/M_\odot \text{ yr}^{-1}) = \log_{10}(L_{\text{IR}}/\text{erg s}^{-1})$ - 43.48. M_{1500} is converted to an un-obscured SFR$_{\text{UV}}$ following Kennicutt (1998): $\log_{10}(\text{SFR}_{\text{UV}}/M_\odot \text{ yr}^{-1})$ = -0.328 (M_{1500}+17.3). The SFRs can be converted to the calibrations in Kennicutt & Evans (2012) that follow a Kroupa IMF by multiplying SFR$_{\text{UV}}$ by a factor 0.63 and multiplying SFR$_{\text{IR}}$ by a factor 0.86.

REFERENCES

Astropy Collaboration, et al. 2013, AAP, 558, A33

Barisic, I., et al. 2017, ApJ, 845, 41

Behrens, C., Pallottini, A., Ferrara, A., Gallerani, S., & Vallini, L. 2018, MNRAS, 477, 552

Bertin, E. 2010, SWarp: Resampling and Co-adding FITS Images Together, Astrophysics Source Code Library, , , ascl:1010.068

Bouwens, R. J., Smit, R., Labbé, I., et al. 2016a, ApJ, 831, 176

Bouwens, R. J., et al. 2012, ApJ, 754, 83

—. 2015, ApJ, 803, 34

—. 2016b, ApJ, 833, 72

Bowler, R. A. A., Bourne, N., Dunlop, J. S., McLure, R. J., & McLeod, D. J. 2018, MNRAS, 481, 1631

Bowler, R. A. A., et al. 2017, MNRAS, 466, 3612

Bradač, M., et al. 2017, ApJL, 836, L2

Capak, P. L., et al. 2015, Nature, 522, 455

Carilli, C. L., & Walter, F. 2013, ARAA, 51, 105

Carniani, S., Maiolino, R., Smit, R., & Amorín, R. 2018a, ApJL, 854, L7

Carniani, S., et al. 2017, AAP, 605, A42

—. 2018b, MNRAS, 478, 1170

Castellano, M., et al. 2017, ApJ, 839, 73

Cen, R., & Kimm, T. 2014, ApJ, 782, 32

Cicone, C., et al. 2015, AAP, 574, A14

Curtis-Lake, E., McLure, R. J., Pearce, H. J., et al. 2012, MNRAS, 422, 1425

da Cunha, E., et al. 2013, ApJ, 766, 13

De Looze, I., et al. 2014, AAP, 568, A62

Decarli, R., et al. 2017, Nature, 545, 457

D'Odorico, V., et al. 2018, ApJL, 863, L29

Erb, D. K., et al. 2014, ApJ, 795, 33

Erwin, P. 2015, ApJ, 799, 226

Faisst, A. L., et al. 2017, ApJ, 847, 21

Ferkinhoff, C., Hailey-Dunsheath, S., Nikola, T., et al. 2010, ApJL, 714, L147

Ferrara, A., Hirashita, H., Ouchi, M., & Fujimoto, S. 2017, MNRAS, 471, 5018

Förster Schreiber, N. M., et al. 2009, ApJ, 706, 1364

Fujimoto, S., Ouchi, M., Ferrara, A., et al. 2019, arXiv e-prints, arXiv:1902.06760

Gil de Paz, A., et al. 2007, ApJS, 173, 185

Harikane, Y., et al. 2018, ApJ, 859, 84

Hashimoto, T., et al. 2017, MNRAS, 465, 1543

—. 2018a, arXiv e-prints, arXiv:1806.00486

—. 2018b, Nature, 557, 392

Hemmati, S., Yan, L., Diaz-Santos, T., et al. 2017, ApJ, 834, 36

Herrera-Camus, R., et al. 2015, ApJ, 800, 1

Hunter, J. D. 2007, Computing in Science and Engineering, 9, 90

Inoue, A. K., et al. 2016, Science, 352, 1559

Jiang, L., Bian, F., Fan, X., et al. 2013, ApJL, 771, L6

Jones, E., Oliphant, T., Peterson, P., et al. 2001–, SciPy: Open source scientific tools for Python, , . http://www.scipy.org/

Jones, G. C., Willott, C. J., Carilli, C. L., et al. 2017, ApJ, 845, 175

Kennicutt, R. C., & Evans, N. J. 2012, ARAA, 50, 531

Kennicutt, Jr., R. C. 1998, ARAA, 36, 189

Knudsen, K. K., Richard, J., Kneib, J.-P., et al. 2016, MNRAS, 462, L6

Table C.1. Observed properties of the galaxy compilation at $z \approx 6-7$. Upper limits are at the 1σ level and in case of [CII] based on the expected line-width from the UV luminosity (Fig. 9).

ID	z	M_{1500}	β	$f_{160\mu m}/\mu Jy$	$L_{[CII]}/10^8\,L_\odot$	$v_{FWHM,[CII]}/km\,s^{-1}$	Reference
A383-5.1	6.029	-19 ± 0.3	-2 ± 0.7	< 11	0.089 ± 0.031	100 ± 23	K16
NTTDF2313	6.07	-21.2		< 18	< 0.21		C18
WMH5	6.075	-22.8		218 ± 41	6.6 ± 0.7	251 ± 15	W15
BDF2203	6.12	-21.5		< 23	1.3 ± 0.3	150 ± 50	C18
CLM1	6.176	-22.7		44 ± 26	2.4 ± 0.3	162 ± 23	W15
GOODS3203	6.27	-21.6		< 41	< 0.59		C18
COSMOS20521	6.36	-21.13	-2.17	< 20	< 0.23		C18
VR7	6.534	-22.4 ± 0.05	-1.4 ± 0.3	< 10.6	4.76 ± 0.14	203 ± 40	This paper
MASOSA	6.543	-20.9 ± 0.1	-1.1 ± 0.7	< 9.2	< 0.22		This paper
UDS4821	6.56	-21.3		< 24	< 0.32		C18
Himiko	6.595	-21.8 ± 0.1	-2 ± 0.4	< 27	1.2 ± 0.2	180 ± 50	C18
CR7	6.604	-22.2 ± 0.1	-2.2 ± 0.4	< 7	3.87 ± 0.65	259 ± 24	M17
COSMOS24108	6.629	-21.67	-1.76 ± 0.2	< 18	1.1 ± 0.15	150 ± 40	P16
UDS16291	6.638	-20.97	-2.4 ± 0.4	< 20	0.7 ± 0.15	50 ± 15	P16
NTTDF6345	6.701	-21.57	-1.3 ± 0.5	< 16	1.8 ± 0.3	250 ± 70	P16
RXJ13471216	6.765	-19.1 ± 0.4	-2.5 ± 0.7	< 15	0.15 ± 0.03	75 ± 25	B17
COS-2987030247	6.807	-22.1 ± 0.1	-1.22 ± 0.5	< 25	3.6 ± 0.5	124 ± 18	L17
SDF-46975	6.844	-21.5		< 19.2	< 0.27		M15
COS-3018555981	6.854	-22 ± 0.1	-1.18 ± 0.5	< 29	4.7 ± 0.5	232 ± 30	S17
IOK-1	6.96	-21.4	-2.07 ± 0.26	< 21	< 0.25		O14
BDF-521	7.008	-20.3		< 17.4	< 0.22		M15
BDF-3299	7.109	-20.9		< 7.8	0.49 ± 0.1	75 ± 20	M15,C17
COSMOS13679	7.145	-21.46	-1.54 ± 0.4	< 14	0.7 ± 0.15	90 ± 35	P16
B14-65666	7.152	-22.3 ± 0.05	-1.85 ± 0.5	130 ± 25	13.3 ± 1.3	349 ± 31	B18,H18
SXDF-NB1006-2	7.212	-21.5	-2.6	< 14	< 0.28		I16

References: B17 (Bradač et al. 2017); B18 (Bowler et al. 2018); C17 (Carniani et al. 2017); C18 (Carniani et al. 2018b); H18 (Hashimoto et al. 2018a); I16 (Inoue et al. 2016); K16 (Knudsen et al. 2016); L17 (Laporte et al. 2017); M15 (Maiolino et al. 2015); M17 (Matthee et al. 2017b); O14 (Ota et al. 2014); P16 (Pentericci et al. 2016); S17(Smit et al. 2018); W15 (Willott et al. 2015)

Konno, A., et al. 2018, PASJ, 70, S16

Laigle, C., et al. 2016, ApJS, 224, 24

Laporte, N., et al. 2017, ApJL, 837, L21

Le Fèvre, O., et al. 2017, arXiv e-prints, arXiv:1710.10715

Maiolino, R., et al. 2015, MNRAS, 452, 54

Maseda, M. V., et al. 2017, AAP, 608, A4

Matthee, J., Sobral, D., Darvish, B., et al. 2017a, MNRAS, 472, 772

Matthee, J., Sobral, D., Gronke, M., et al. 2018, AAP, 619, A136

Matthee, J., Sobral, D., Oteo, I., et al. 2016, MNRAS, 458, 449

Matthee, J., Sobral, D., Santos, S., et al. 2015, MNRAS, 451, 400

Matthee, J., et al. 2017b, ApJ, 851, 145

Meurer, G. R., Heckman, T. M., & Calzetti, D. 1999, ApJ, 521, 64

Nakajima, K., Ellis, R. S., Iwata, I., et al. 2016, ApJL, 831, L9

Olsen, K., Greve, T. R., Narayanan, D., et al. 2017, ApJ, 846, 105

Ono, Y., Ouchi, M., Shimasaku, K., et al. 2010, ApJ, 724, 1524

Ota, K., et al. 2014, ApJ, 792, 34

Ouchi, M., et al. 2013, ApJ, 778, 102

Table C.2. Derived properties of the galaxy compilation at $z \approx 6 - 7$, based on the measurements listed in Table *C*.1. SFRs are based on the calibrations presented in Kennicutt (1998). Infrared luminosities have been corrected for CMB-heating following da Cunha et al. (2013). Upper limits are at the 1σ level.

ID	$\mathrm{SFR_{UV}/M_\odot \ yr^{-1}}$	$\mathrm{L_{IR,Td=35K}/10^{10} \ L_\odot}$	$\mathrm{L_{IR,Td=45K}/10^{10} \ L_\odot}$	$\mathrm{SFR_{IR,Td=45K}/M_\odot \ yr^{-1}}$
A383-5.1	3.5 ± 0.9	< 1.2	< 2.4	< 4.2
NTTDF2313	19.0	< 2.0	< 4.0	< 6.9
WMH5	63.6	24.0 ± 4.5	48.2 ± 8.9	83.9 ± 15.6
BDF2203	23.8	< 2.6	< 5.1	< 9.0
CLM1	59.0	5.0 ± 2.7	10.0 ± 5.6	17.4 ± 9.8
GOODS3203	25.7	< 4.8	< 9.6	< 16.6
COSMOS20521	18.0	< 2.4	< 4.8	< 8.3
VR7	47.1 ± 1.7	< 1.3	< 2.6	< 4.6
MASOSA	15.0 ± 2.0	< 1.2	< 2.3	< 4.0
UDS4821	20.5	< 3.1	< 6.1	< 10.5
Himiko	29.9 ± 2.2	< 3.5	< 6.9	< 12.0
CR7	40.7 ± 3.2	< 0.9	< 1.8	< 3.1
COSMOS24108	27.1	< 2.3	< 4.6	< 8.1
UDS16291	16.0	< 2.6	< 5.2	< 9.0
NTTDF6345	25.1	< 2.1	< 4.2	< 7.3
RXJ13471216	4.0 ± 1.2	< 2.0	< 4.0	< 7.0
COS-2987030247	37.4 ± 3.0	< 3.4	< 6.7	< 11.7
SDF-46975	23.8	< 2.7	< 5.2	< 9.1
COS-3018555981	34.7 ± 2.6	< 4.0	< 7.9	< 13.8
IOK-1	22.1	< 3.0	< 5.9	< 10.3
BDF-521	9.6	< 2.5	< 4.9	< 8.6
BDF-3299	15.1	< 1.2	< 2.3	< 4.0
COSMOS13679	23.1	< 2.1	< 4.1	< 7.2
B14-65666	43.3 ± 1.6	19.8 ± 3.9	38.3 ± 7.6	66.7 ± 13.3
SXDF-NB1006-2	23.8	< 2.2	< 4.2	< 7.3

Pentericci, L., et al. 2016, ApJL, 829, L11

Raiter, A., Fosbury, R. A. E., & Teimoorinia, H. 2010a, AAP, 510, A109

Raiter, A., Schaerer, D., & Fosbury, R. A. E. 2010b, AAP, 523, A64

Reddy, N. A., et al. 2018, ApJ, 853, 56

Rémy-Ruyer, A., et al. 2013, AAP, 557, A95

—. 2015, AAP, 582, A121

Rigby, J. R., Bayliss, M. B., Gladders, M. D., et al. 2015, ApJ, 814, L6

Salpeter, E. E. 1955, ApJ, 121, 161

Schaerer, D., Boone, F., Zamojski, M., et al. 2015, AAP, 574, A19

Schaerer, D., & de Barros, S. 2009, AAP, 502, 423

Shapley, A. E., Steidel, C. C., Pettini, M., & Adelberger, K. L. 2003, ApJ, 588, 65

Shibuya, T., Ouchi, M., & Harikane, Y. 2015, ApJS, 219, 15

Shibuya, T., et al. 2018, PASJ, 70, S15

Smit, R., Bouwens, R. J., et al. 2018, Nature, 553, 178

Smit, R., et al. 2014, ApJ, 784, 58

Sobral, D., & Matthee, J. 2019, arXiv e-prints, arXiv:1803.08923

Sobral, D., Matthee, J., Darvish, B., et al. 2015, ApJ, 808, 139

Sobral, D., et al. 2018, MNRAS, 477, 2817

—. 2019, mnras, 482, 2422

Stacey, G. J., Geis, N., Genzel, R., et al. 1991, ApJ, 373, 423

Stark, D. P., et al. 2015, MNRAS, 450, 1846

Table C.3. Lyman-α properties of the galaxy compilation at $z \approx 6 - 7$.

ID	$L_{Ly\alpha}/10^{42}$ erg s^{-1}	$EW_{0,Ly\alpha}/Å$	$\Delta v_{Ly\alpha}/$km s^{-1}
A383-5.1	7	138	90±20
NTTDF2313			
WMH5		13	265±52
BDF2203		3	
CLM1		50	430±69
GOODS3203		5	
COSMOS20521	3	10	
VR7	24	34	217±25
MASOSA	24	145	
UDS4821		48	
Himiko	43	65	145±15
CR7	83	211	167±27
COSMOS24108	10	27	240±0
UDS16291	0.8	6	110±0
NTTDF6345	4	15	110±0
RXJ13471216	6	26	20±90
COS-2987030247	5	16	326±30
SDF-46975	15	43	
COS-3018555981			
IOK-1		42	
BDF-521		64	
BDF-3299	7	50	64±10
COSMOS13679	13	28	135±0
B14-65666	2.6	4	772±45
SXDF-NB1006-2		33	

Steinhardt, C. L., et al. 2014, ApJL, 791, L25

Stroe, A., Sobral, D., Matthee, J., Calhau, J., & Oteo, I. 2017, MNRAS, 471, 2558

Tamura, Y., et al. 2018, arXiv e-prints, arXiv:1806.04132

Taylor, M. 2013, Starlink User Note, 253

Trainor, R. F., Strom, A. L., Steidel, C. C., & Rudie, G. C. 2016, ApJ, 832, 171

Vallini, L., Ferrara, A., Pallottini, A., & Gallerani, S. 2017, MNRAS, 467, 1300

Vallini, L., Gallerani, S., Ferrara, A., & Baek, S. 2013, MNRAS, 433, 1567

Vallini, L., Gallerani, S., Ferrara, A., Pallottini, A., & Yue, B. 2015, ApJ, 813, 36

Walter, F., et al. 2018, ApJL, 869, L22

Wang, R., et al. 2013, ApJ, 773, 44

Willott, C. J., Carilli, C. L., Wagg, J., & Wang, R. 2015, ApJ, 807, 180

Wolfire, M. G., McKee, C. F., Hollenbach, D., & Tielens, A. G. G. M. 2003, ApJ, 587, 278